

正电子概况IV

正电子技术及其发展

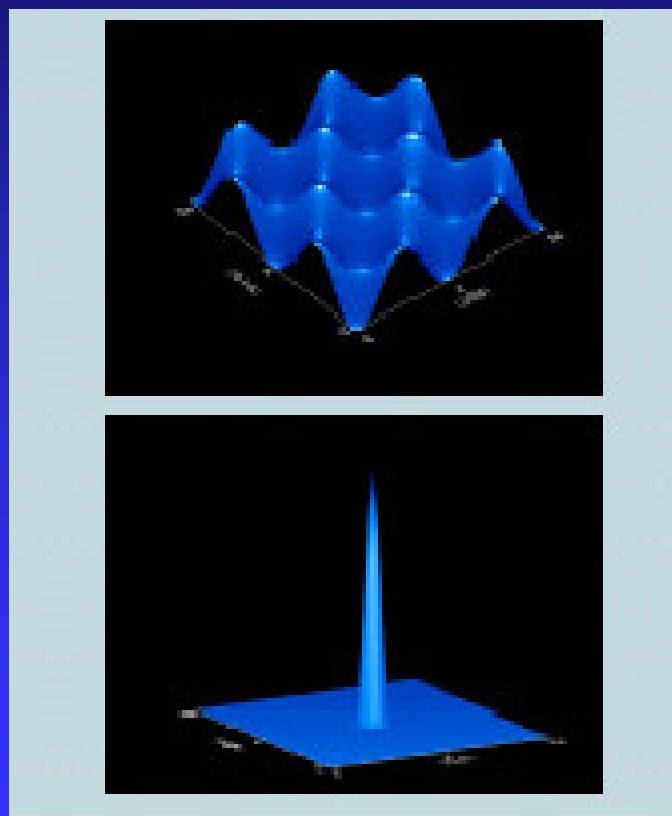
叶邦角



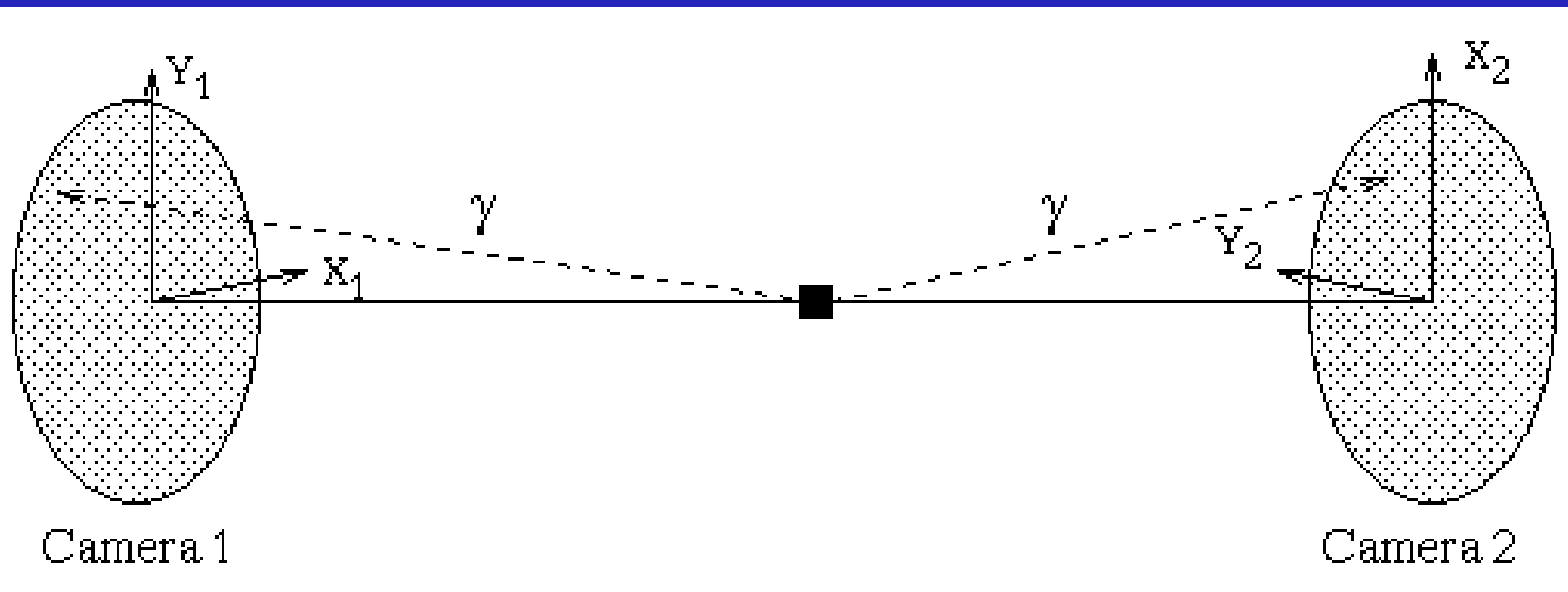
核固体物理研究室

Laboratory of Nuclear Solid
State Physics, USTC

5.正电子角关联



- $e+e^-$ 湮没产生的 2γ 的夹角与 180° 有一微小的偏离。实验同时测量 $e+e^-$ 湮没产生的 2γ 关联信号，可以获得电子动量分布信息，并且可进一步得到费米面形貌，研究能带结构等。
- 同CDB相似，二维角关联（2D-ACAR）可以由 $e+e^-$ 湮灭的动量分布来获得电子结构的信息，特别对单晶材料。



- 比之CDB技术，2D-ACAR技术具有以下两个优点：

(1) 可以获得更多的信息，因为是二维探测，故动量密度仅仅积分一次，即：

$$N(p_x, p_y) = \int \rho^{2\gamma}(\vec{p}) dp_z$$

而多普勒展宽技术主要是一维探测，故取的是两次积分后的信息，即：

$$D(p_z) = \iint \rho^{2\gamma}(\vec{p}) dp_y dp_x$$

(2) **2D-ACAR**比多普勒展宽技术具有更高的分辨。

通常2D-ACAR技术具有 $0.5 \times 10^{-3} m_e c$ 量级的分辨，而CDB的分辨为 $4 \times 10^{-3} m_e c$ 。

2D-ACAR技术的主要缺点是必须有较多的计数，因而需要较强的正电子源强并且需要较长的测量时间，此外它经常要与寿命谱仪和多普勒展宽技术联合使用。

Principle of the Momentum Distribution Techniques

The momentum components $p_{x,y}$ perpendicular to the propagation direction lead to angular deviations $\Theta_{x,y}$ of the collinearity of the annihilation γ -rays according to

$$\Theta_{x,y} = \frac{p_{x,y}}{m_0 c}$$

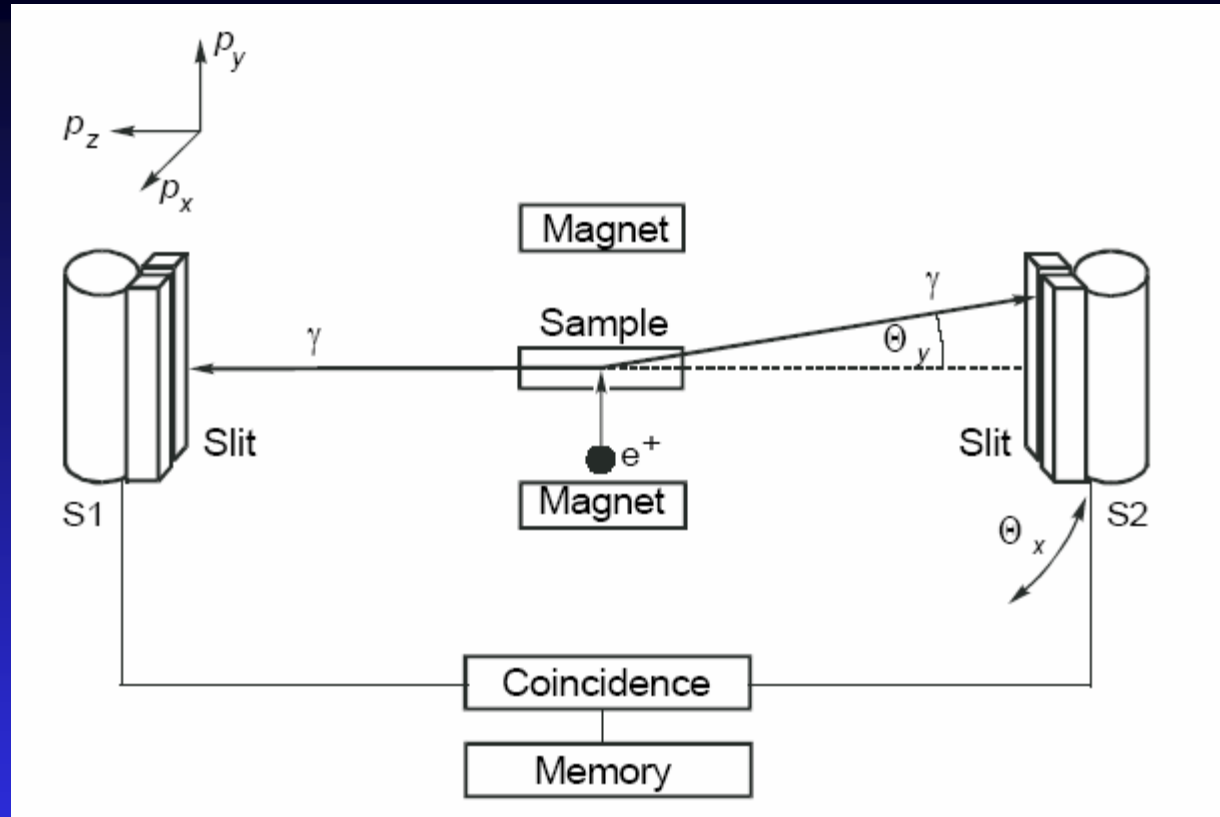
These equations hold for small angles. $\Theta_{x,y}$ can be registered simultaneously in both x and y directions by a coincidence measurement using position-sensitive detection of the γ -quanta.

- Due to the limited energy resolution of Doppler-broadening spectroscopy, electron structure investigations are carried out mainly by angular correlation of annihilation radiation.
- Because the momentum of valence electrons is significantly lower, the momentum distribution of annihilating electrons shifts to smaller values. This means a smaller angular deviation for ACAR and a smaller Doppler broadening for DOBS.
- The curve of defect-rich material is thus higher and narrower than that of defect-free reference material, when both curves are normalized to equal area.

1D-ACAR

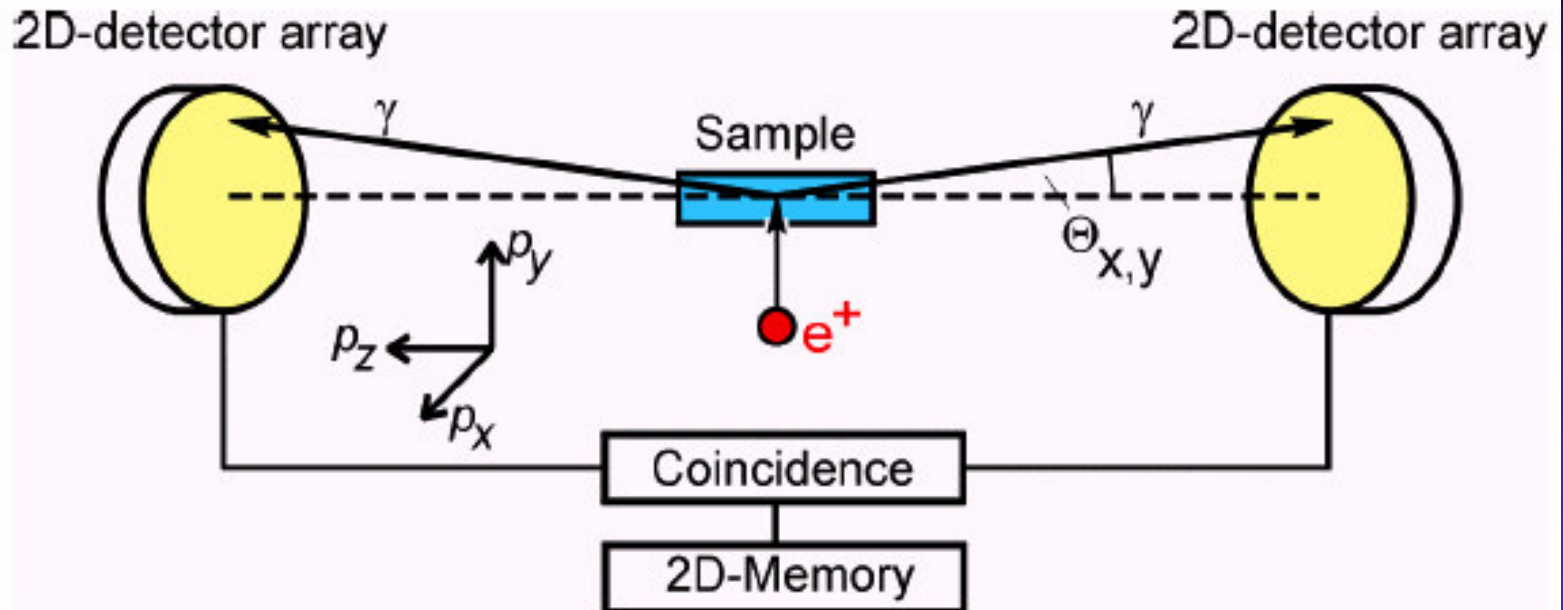
- The first ACAR measurements in one dimension were realized with Geiger counters by Behringer and Montgomery (1942). A position-sensitive detection can be realized in the simplest way in one dimension (1D-ACAR) by the mechanical movement of a long scintillation detector (Hautojärvi and Vehanen 1979; Mijnaerends 1979). The integration in one more dimension compared with (6) results in a counting rate of

$$N_c(\Theta_x) = A_c \int_{-\infty}^{\infty} \int_{-\infty}^{\infty} \sigma(\Theta_x m_0 c, p_y, p_z) dp_y dp_z .$$



The angular resolution is realized by lead slits . It can be adjusted in the range 0.2 to 5 mrad. The energy resolution of a corresponding Doppler broadening experiment would range from 0.05 to 1.3 keV. Thus, ACAR has a much better momentum resolution than the Doppler-broadening technique.

2D-ACAR



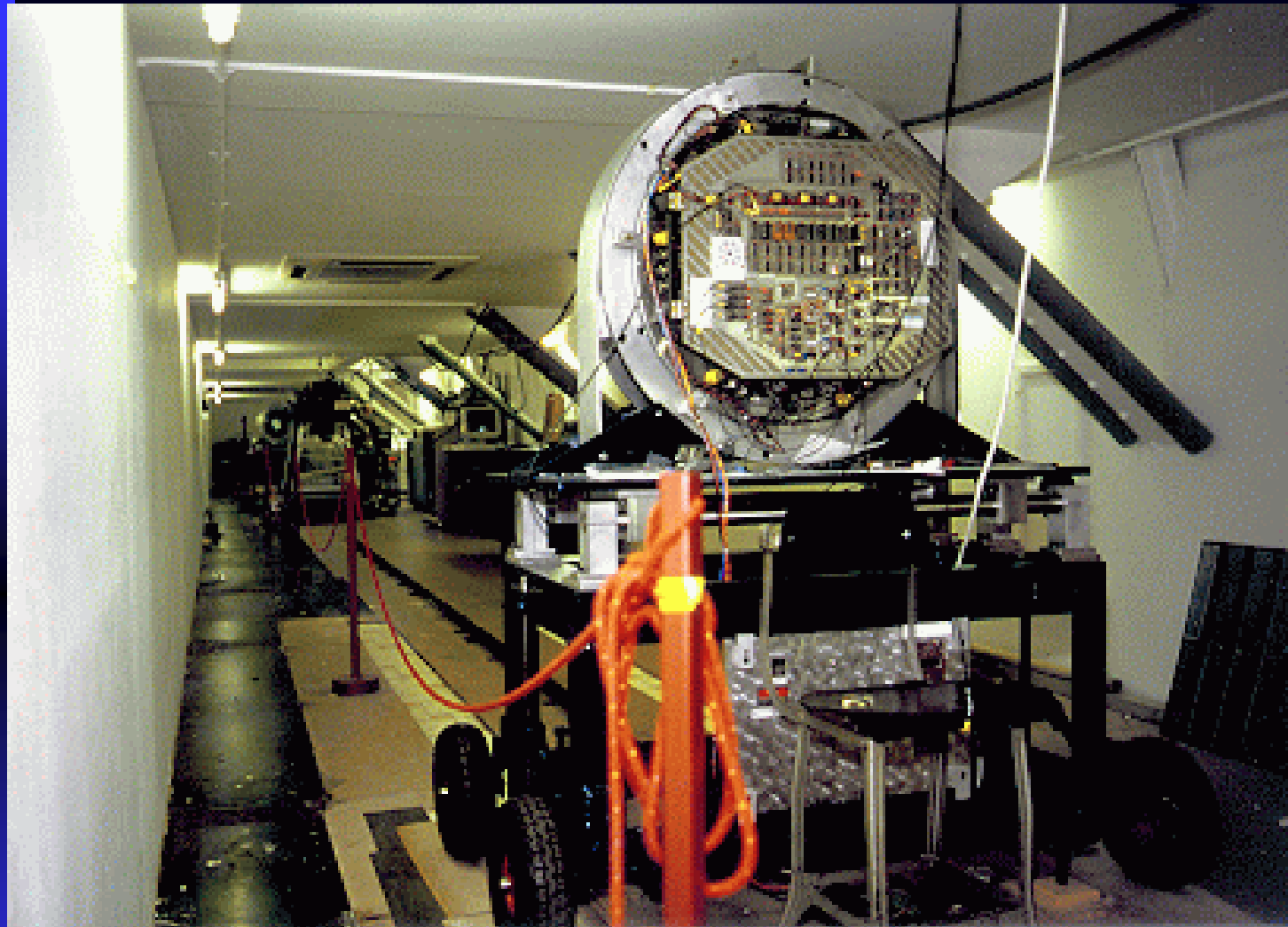
Coincidence counting rate N_c :

$$N_c(\Theta_x, \Theta_y) = A_c \int \bar{\sigma}(\Theta_x m_0 c, \Theta_y m_0 c, p_z) dp_z$$

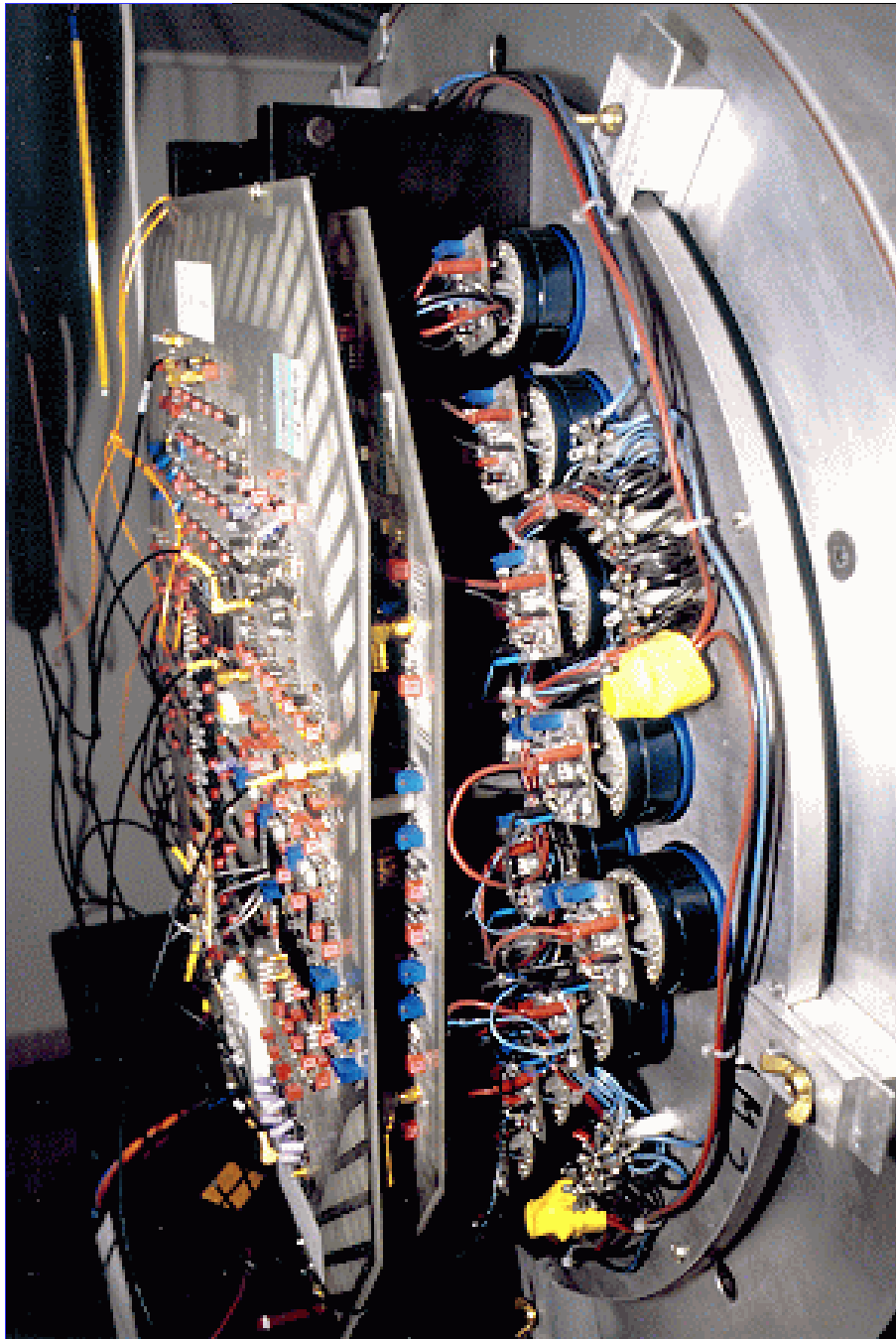
$$\Theta_{x,y} = p_{x,y} / m_0 c$$

Resolution: 0.2~5mrad (0.05~1.2keV)

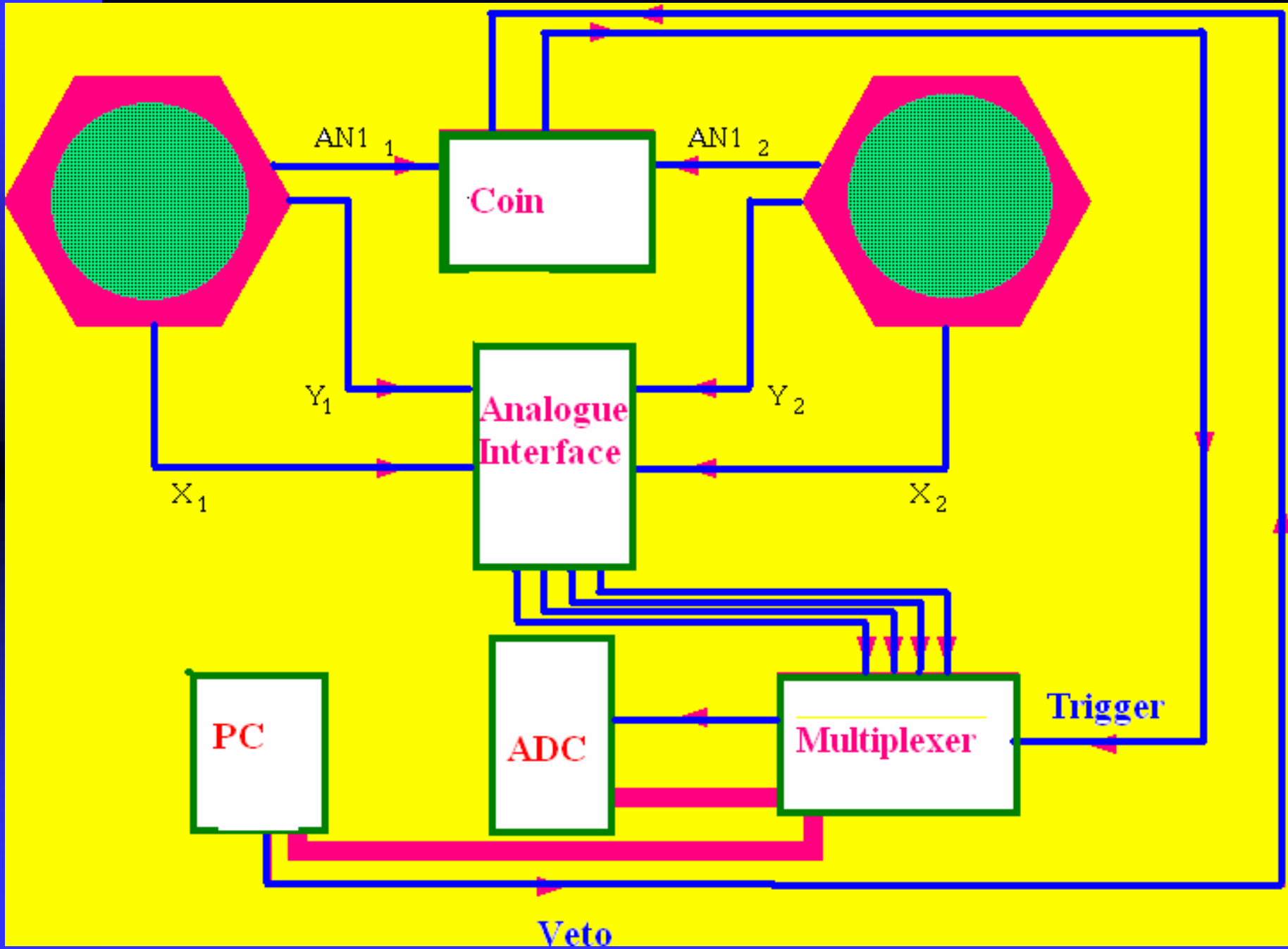


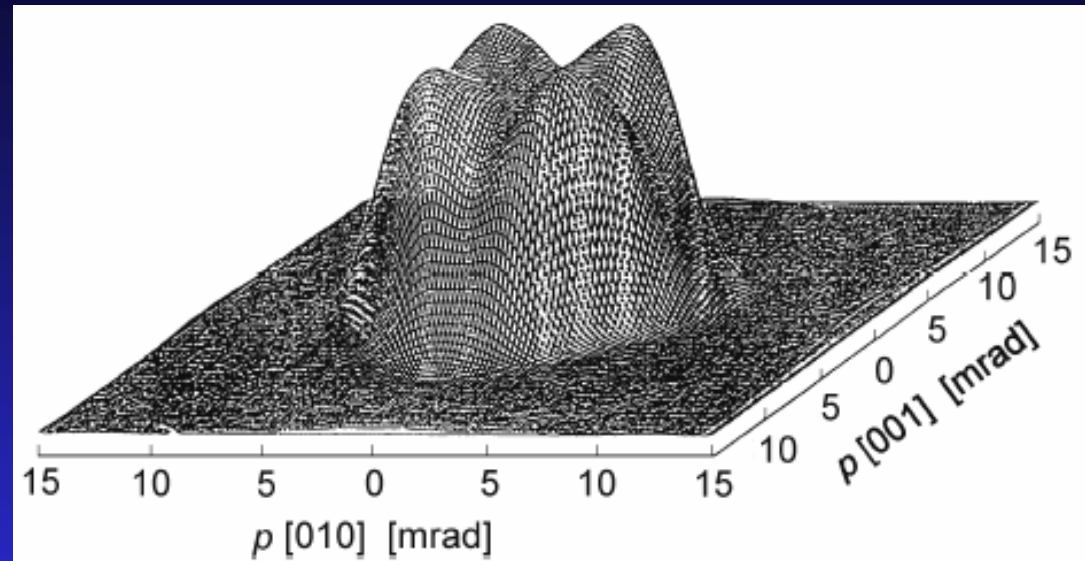
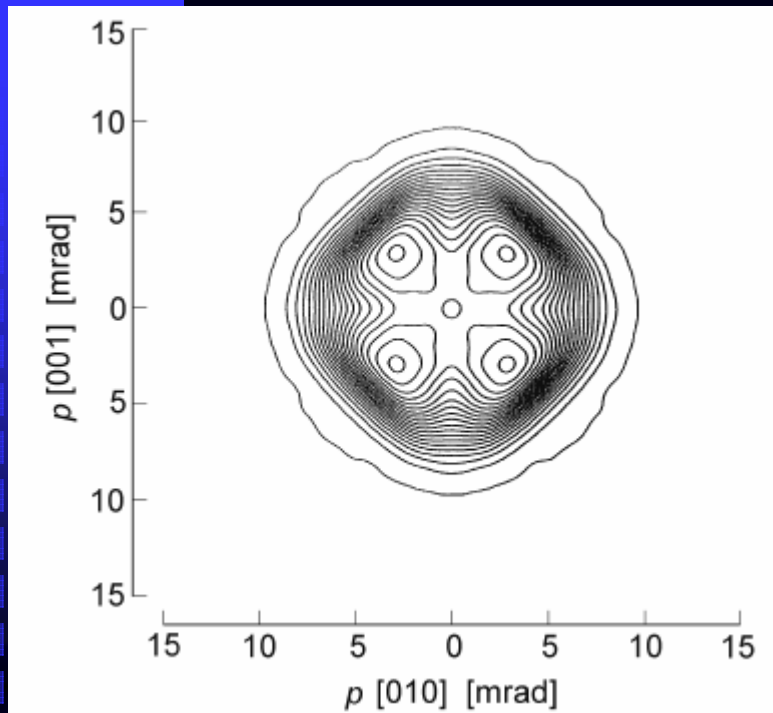


- The 'long laboratory', showing one of the position sensitive gamma-ray detectors known as 'Anger Cameras'

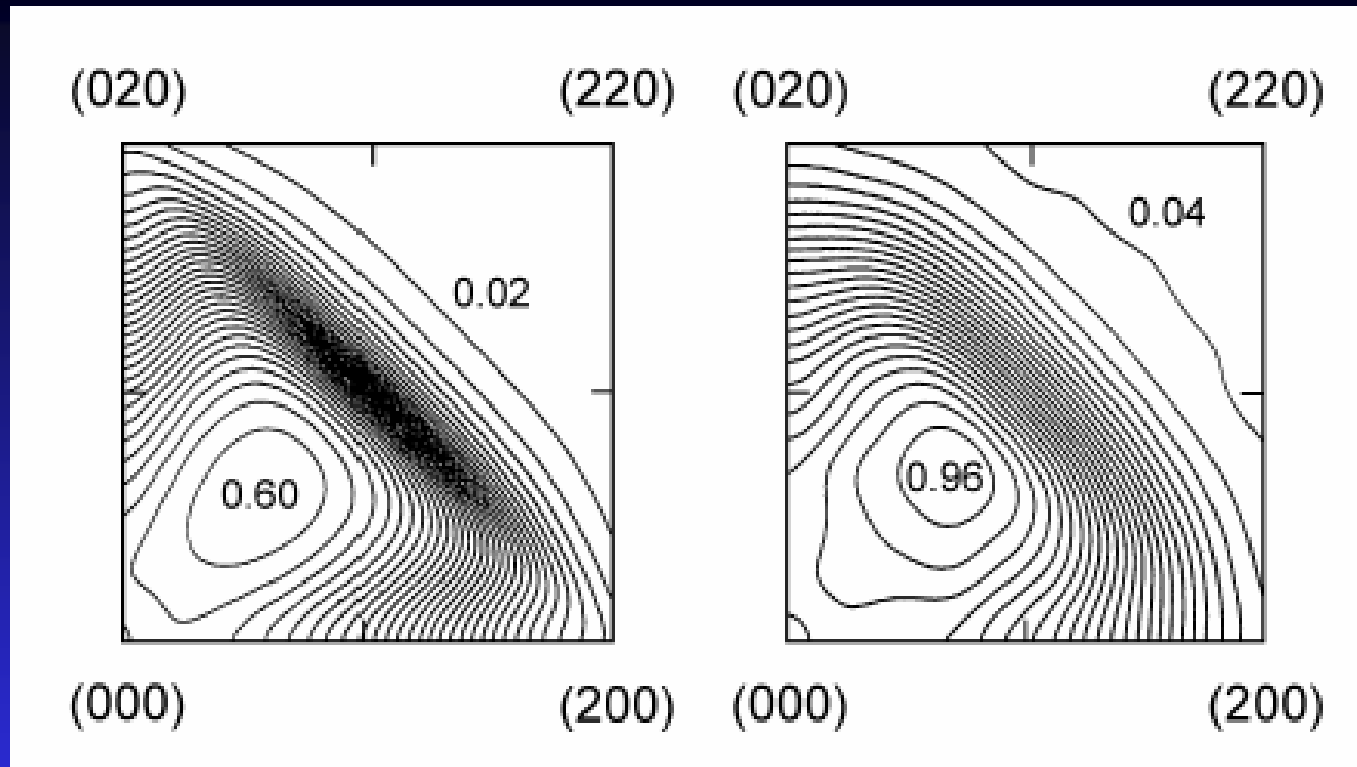


- Close-up of one of the Anger cameras. The individual photomultiplier tubes can clearly be seen.





Combined perspective and contour plots of the measurement of two-dimensional angular correlation of annihilation radiation in gallium arsenide exhibiting no positron trapping in defects (Tanigawa et al. 1995). The upper panel shows the contour map of the momentum distribution p in the (100) plane.



Comparison of the two-dimensional angular correlation of annihilation radiation contour plot of the momentum distribution in the (001) plane of gallium arsenide obtained by *ab-initio* calculations (*left panel*) by Saito et al. (1991) with an experimental spectrum (*right panel*). The right panel represents a magnified part of the contour plot of Fig..

PHYSICAL REVIEW B **66**, 075426 (2002)

Electronic structure and orientation relationship of Li nanoclusters embedded in MgO studied by depth-selective positron annihilation two-dimensional angular correlation

C. V. Falub

Interfaculty Reactor Institute, Delft University of Technology, Mekelweg 15, NL-2629 JB Delft, The Netherlands

P. E. Mijnarends

*Interfaculty Reactor Institute, Delft University of Technology, Mekelweg 15, NL-2629 JB Delft, The Netherlands
and Department of Physics, Northeastern University, Boston, Massachusetts 02115*

S. W. H. Eijt, M. A. van Huis, A. van Veen, and H. Schut

Interfaculty Reactor Institute, Delft University of Technology, Mekelweg 15, NL-2629 JB Delft, The Netherlands

(Received 26 March 2002; published 30 August 2002)

- A 2D-ACAR setup coupled to the intense ($8 \times 10^7 e^+/s$) monochromatic slow e^+ beam POSH (POSitrons from the HOR reactor) is used for depth-selective research.
- The Anger cameras, used to detect the 511-keV γ radiation stemming from the annihilation of positrons in the sample, consist of 41.8-cm-diameter 1.25-cm thick NaI crystal scintillators, optically coupled to a close packed honeycomb array of 61 photomultipliers. A detector-detector distance of ~ 23 m provides an angular view of $\sim 51 \times 51$ mrad² (1 mrad is equivalent to 0.137 momentum a.u.) in a 256×256 pixel matrix.

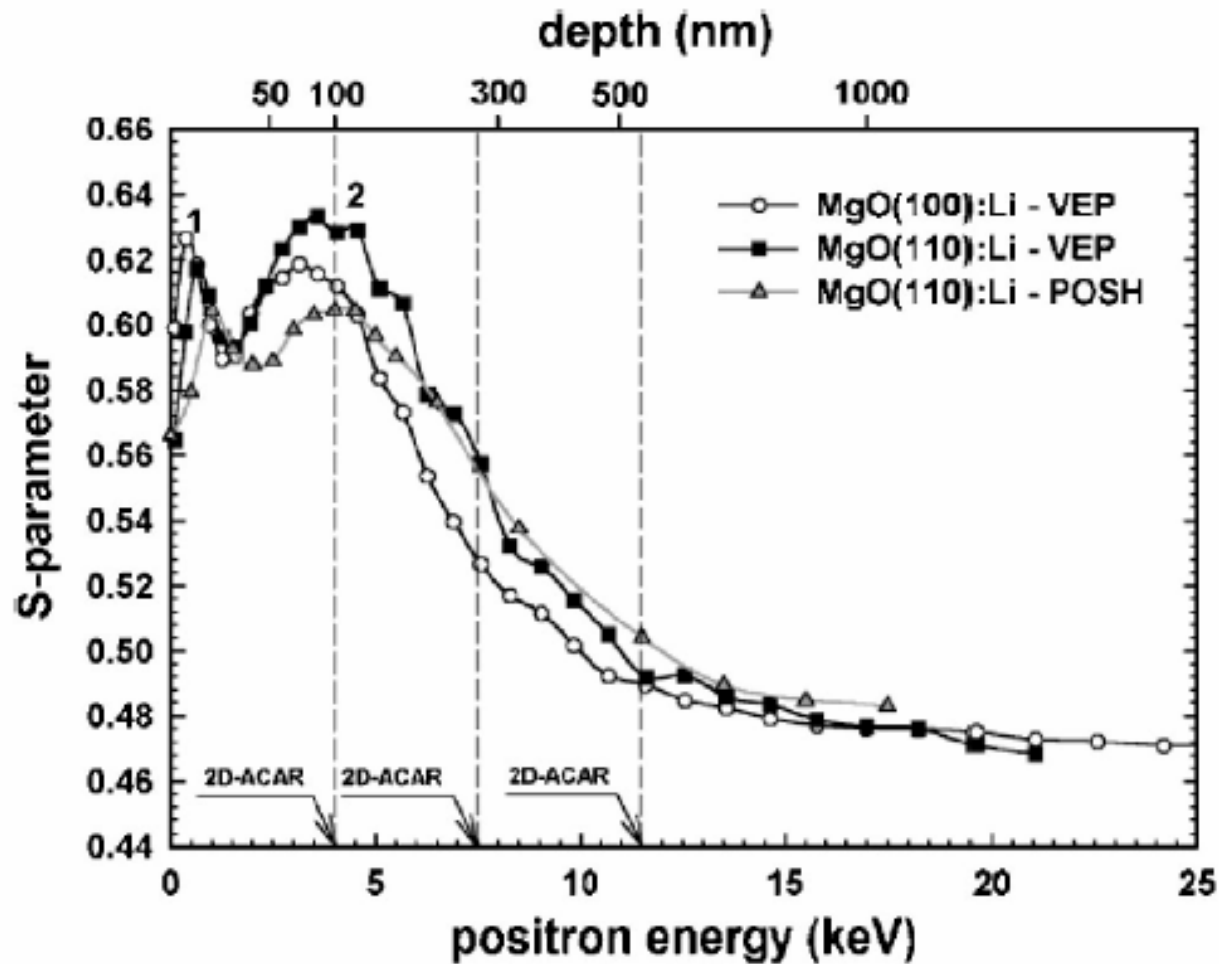
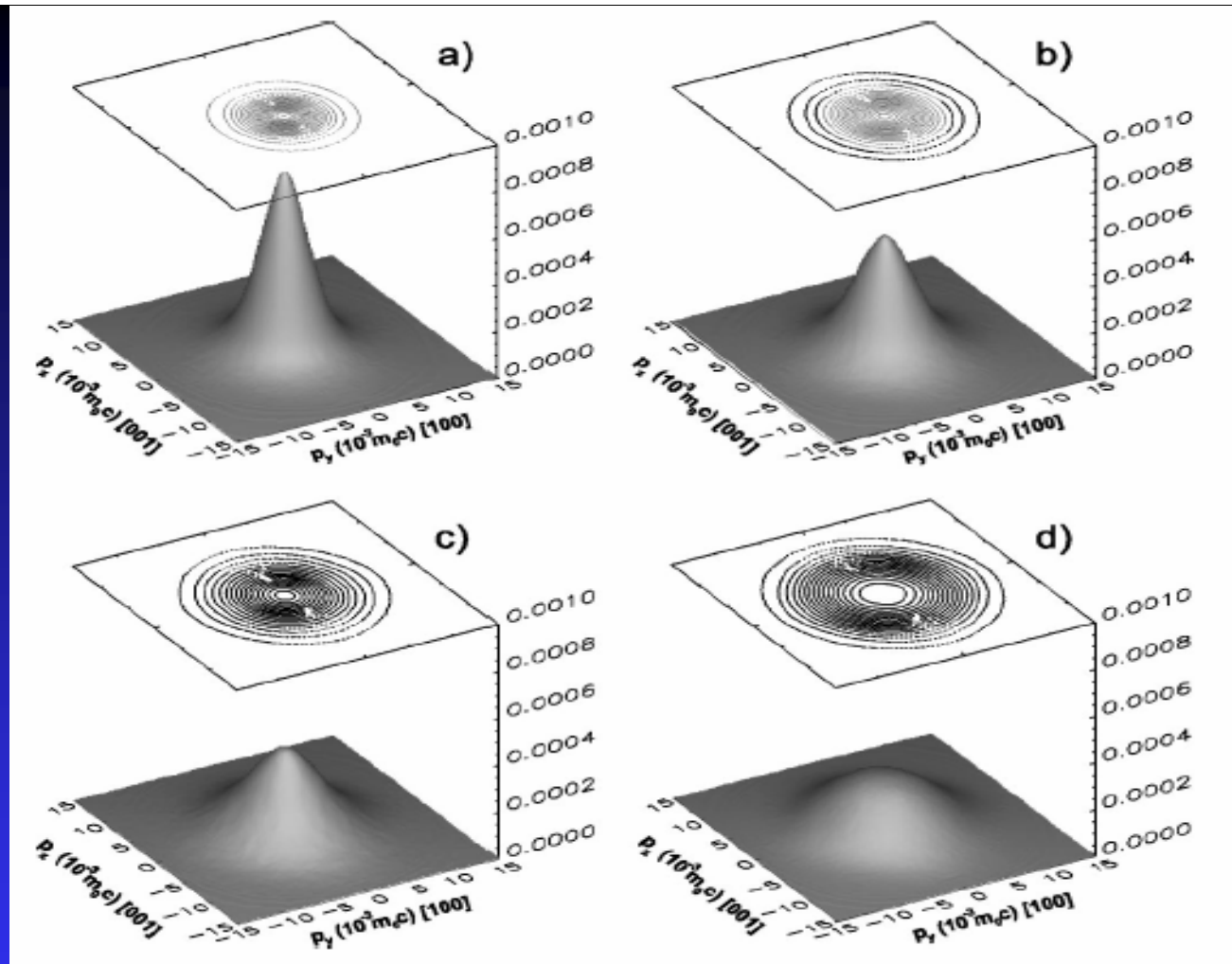


FIG. 2. *S* parameter vs positron implantation energy for Li implanted MgO(100) and MgO(110). Peak 1 corresponds to the Al layer; peak 2 to the Li implantation range.

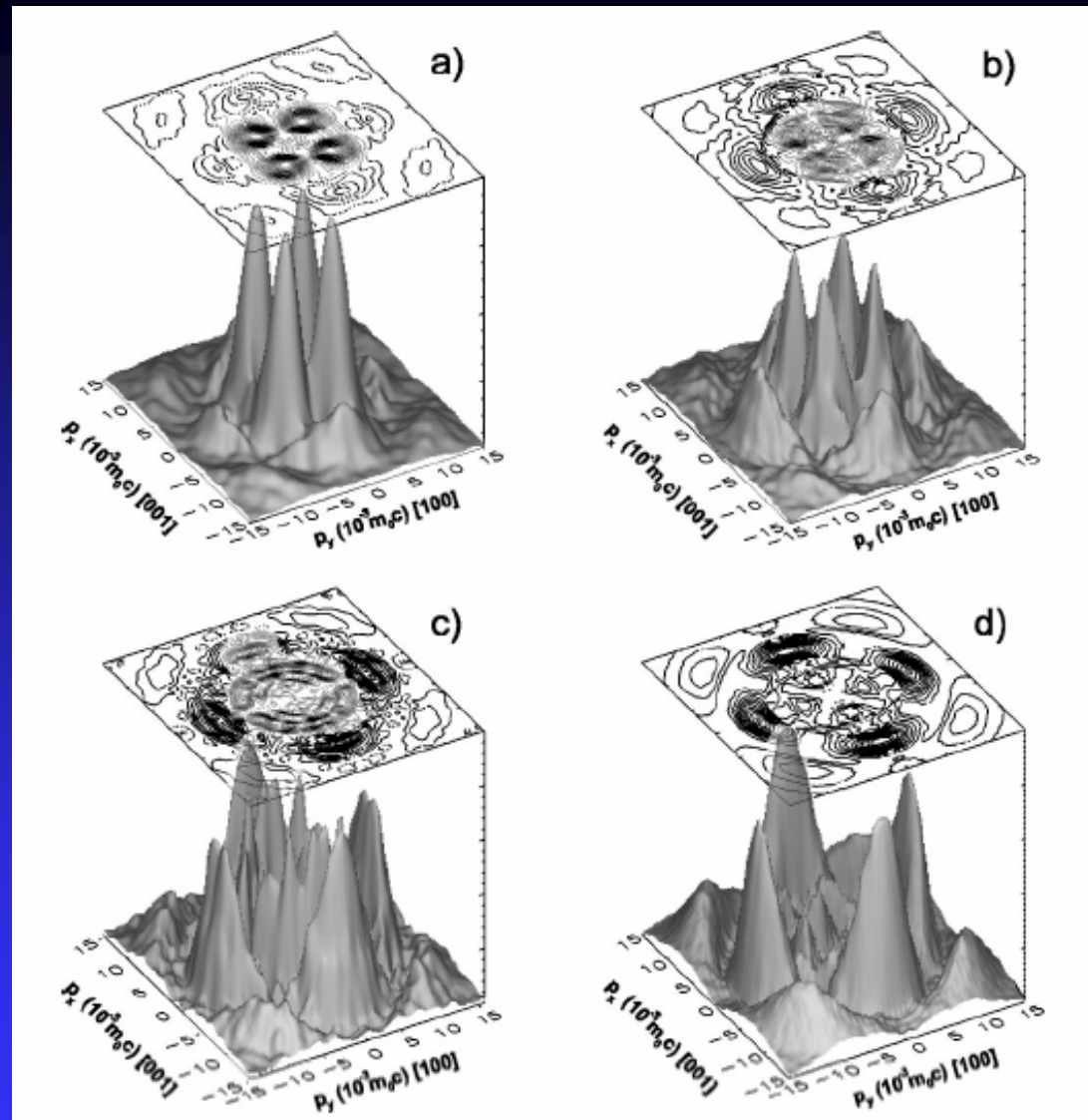
VEP (a ^{22}Na based slow positron beam)

- A detailed analysis by means of the fitting code VEPFIT has shown that the S parameter curves depicted in Fig. 2 can be fitted very well with a model consisting of five layers:
- An Al top layer,
- An intermediate MgO layer,
- A Li implantation layer (MgO:Li),
- A layer with the Li implantation tail,
- the MgO bulk.



2D-ACAR distributions for Li implanted MgO(100) at positron energies of (a) 4 keV, (b) 7.5 keV, and (c) 11.5 keV; (d) 2D-ACAR spectrum for bulk MgO(100). The distributions are normalized to equal total numbers of counts..

- The energy corresponding to optimum implantation in the lithium layer(MgO:Li) is ~ 4 keV.
- It is clear that the 4-keV spectrum is much sharper than the bulk spectrum, consistent with the DBAR results, which show a strong increase of the S parameter in the Li implantation range. This increase is correlated with the formation of Li nanoclusters in MgO.
- The 7.5-keV spectrum is still sharp compared to the bulk spectrum, thus showing that at 7.5 keV the contribution of the Li nanoclusters is significant.
- In the 11.5-keV spectrum this contribution, although weak, is still present, but the spectrum resembles more the bulk spectrum.



Anisotropy of the 2D-ACAR distributions in Fig. 3. The distributions are symmetrized and normalized to equal total numbers of counts.

- The anisotropic part of each 2D-ACAR spectrum in Fig. 3 was determined by subtracting a radially smoothed isotropic distribution that remains everywhere within the measured spectrum.
- The anisotropy is therefore everywhere positive.
- One observes a large difference between the anisotropy of the 4-keV and the bulk distribution.
- In the 4-keV 2D-ACAR spectrum the bulk MgO(100) anisotropy is still visible, but the main contribution consists of four prominent peaks positioned at a radius of $4.1 \times 10^{23} m_0 c$, i.e., near the Fermi radius of lithium.
- The Li nanoclusters are coherent or semicoherent with the MgO(100) host matrix since the anisotropic contributions displayed in Figs. 4(a) and 4(d) have the same symmetry and identical mirror planes.

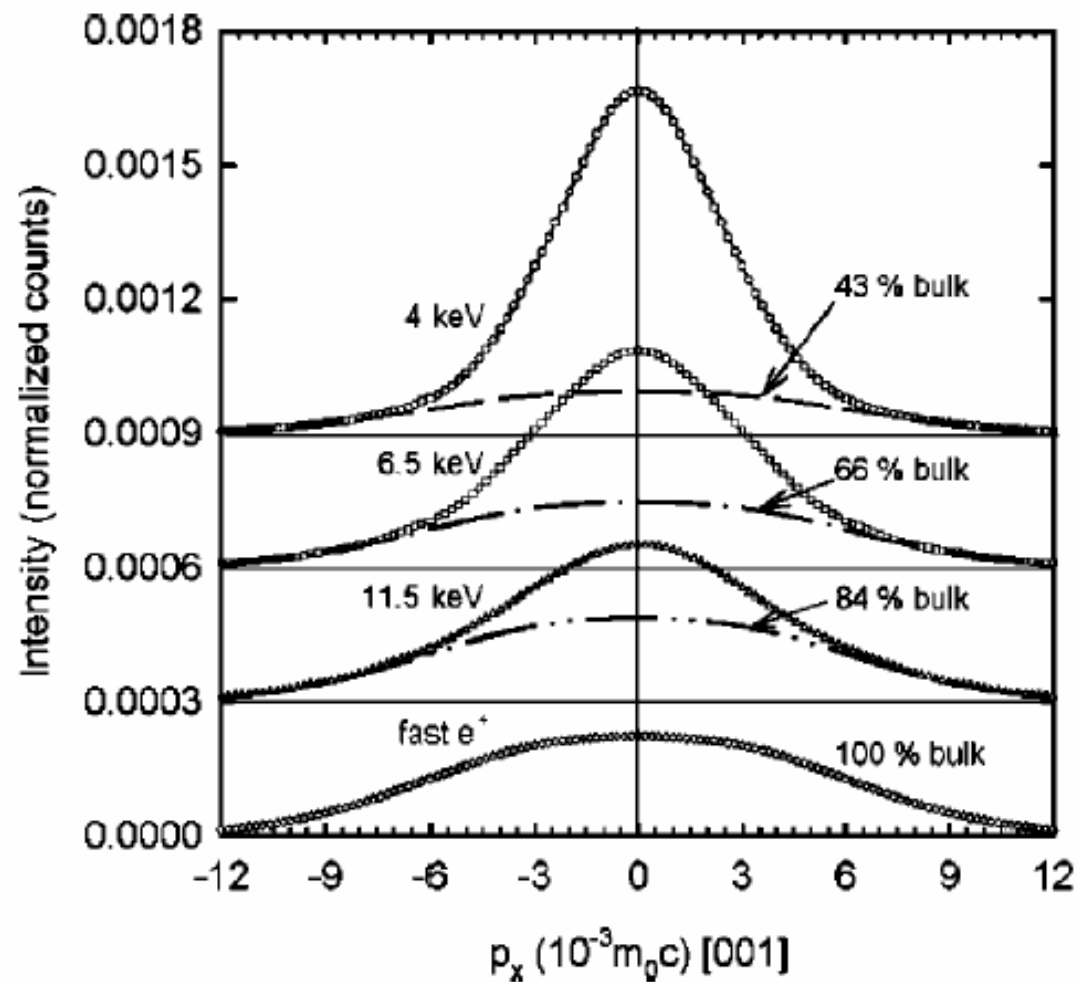
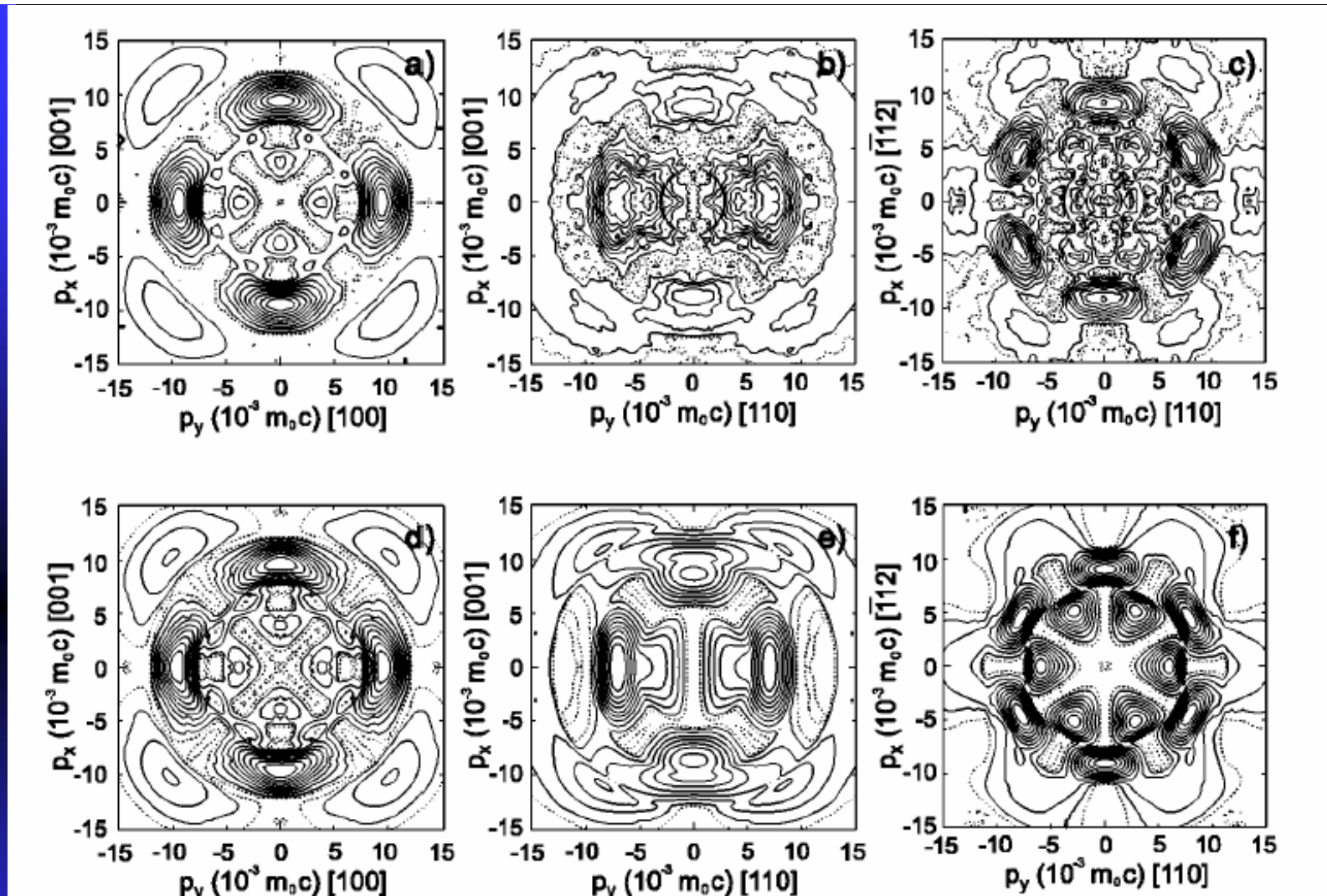
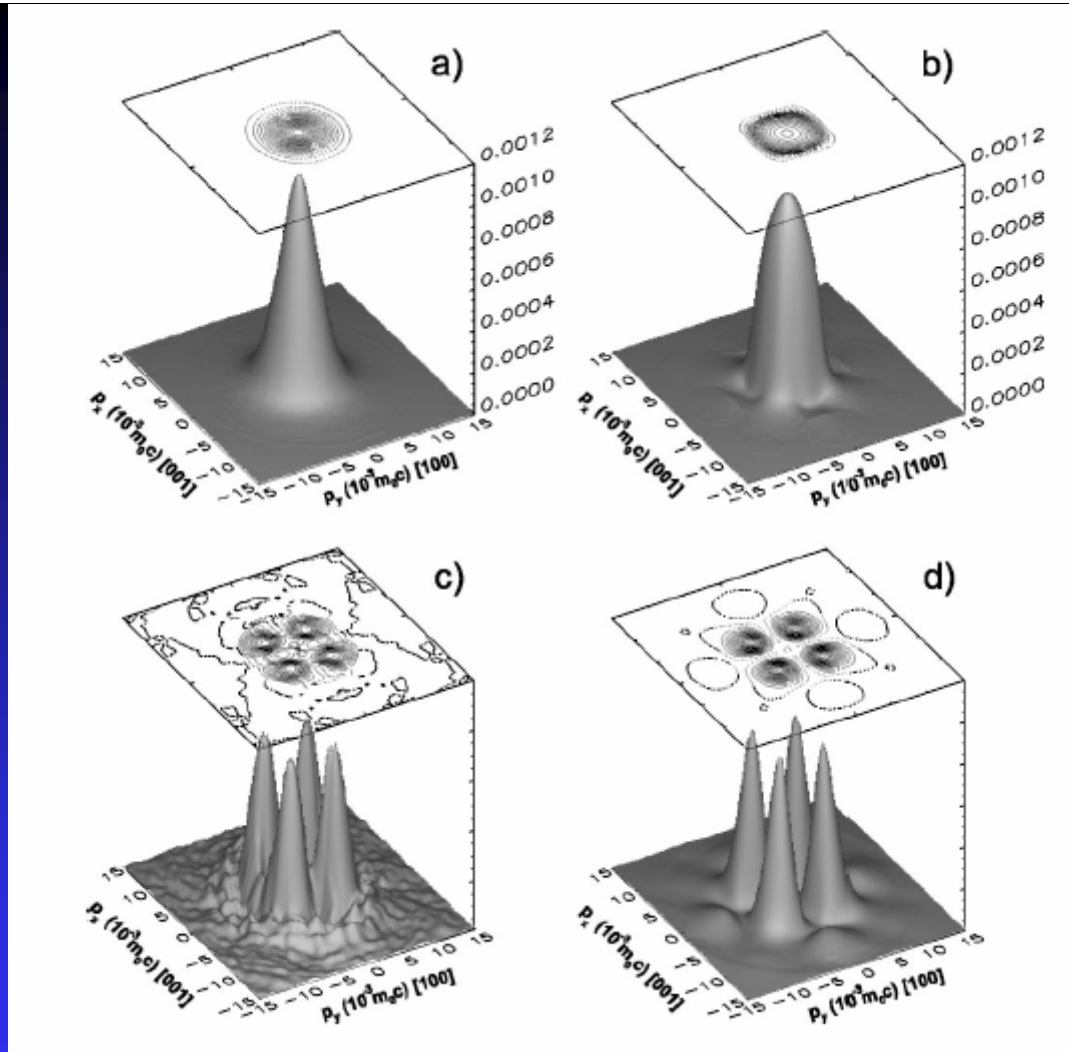


FIG. 5. Cross sections along p_x of the 2D-ACAR distributions for Li implanted MgO at a few positron implantation energies. The cross section of the bulk 2D-ACAR distribution obtained with fast positrons from a ^{22}Na source, and the bulk fractions are also shown. The cross sections are normalized to the total number of counts in the distributions.



Anisotropy in the 2DACAR distributions of MgO measured with fast positrons, corresponding to the projections along the (a) [010], (b) [110], and (c) [111] directions. Parts (d), (e), and (f) show the corresponding results of KKR theory.



(a) Experimental 2D-ACAR distribution after subtracting the bulk MgO(100) contribution (43%); (b) theoretical spectrum of fcc Li(100); (c) and (d) anisotropies of the distributions in (a) and (b). The distributions are normalized with respect to the total number of counts.

Fermi Surface of Nanocrystalline Embedded Particles in Materials: bcc Cu in Fe

Y. Nagai,¹ T. Chiba,² Z. Tang,³ T. Akahane,² T. Kanai,¹ M. Hasegawa,^{1,3} M. Takenaka,⁴ and E. Kuramoto⁴

¹*The Oarai Branch, Institute for Materials Research, Tohoku University, Oarai, Ibaraki 311-1313, Japan*

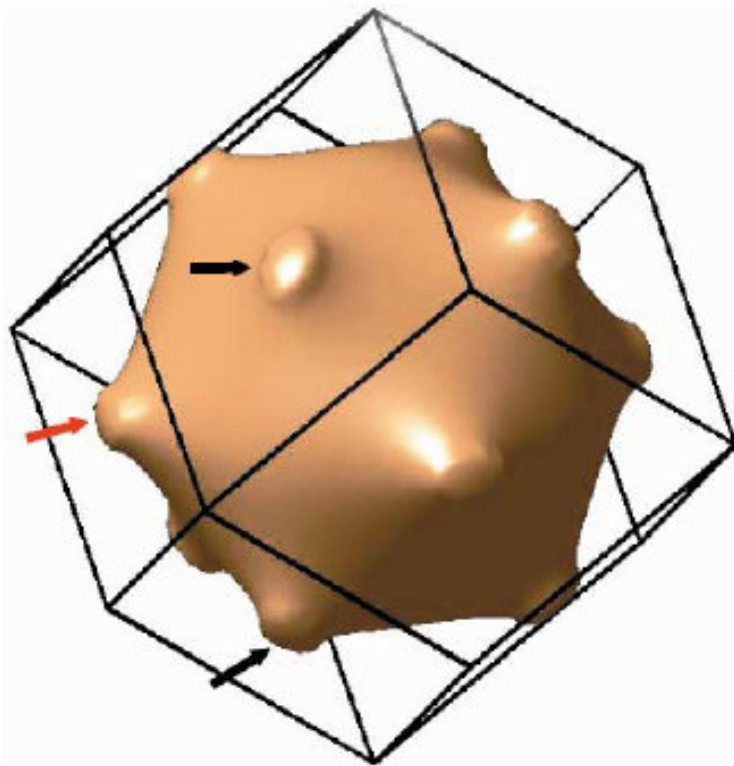
²*Advanced Materials Laboratory, National Institute for Materials Science, Tsukuba 305-0044, Japan*

³*Institute for Materials Research, Tohoku University, Sendai 980-8577, Japan*

⁴*Research Institute for Applied Mechanics, Kyushu University, Fukuoka 816-8580, Japan*

(Received 19 March 2001; published 5 October 2001)

We report that a positron can act as a probe to directly reveal electronic structures of nanocrystalline embedded particles in materials. The Fermi surface (FS) of “bcc” Cu nanoparticles in an Fe matrix is observed as the first example. A two-dimensional angular correlation of the positron annihilation radiation (2D-ACAR) method is used to measure the momentum distribution which reflects the FS topology. The obtained 2D-ACAR spectra show strong and characteristic anisotropy associated with the necks of the FS around the $\{110\}$ Brillouin zone boundaries of the bcc Cu, which are well reproduced by full-potential linearized augmented plane-wave calculations.



(a)

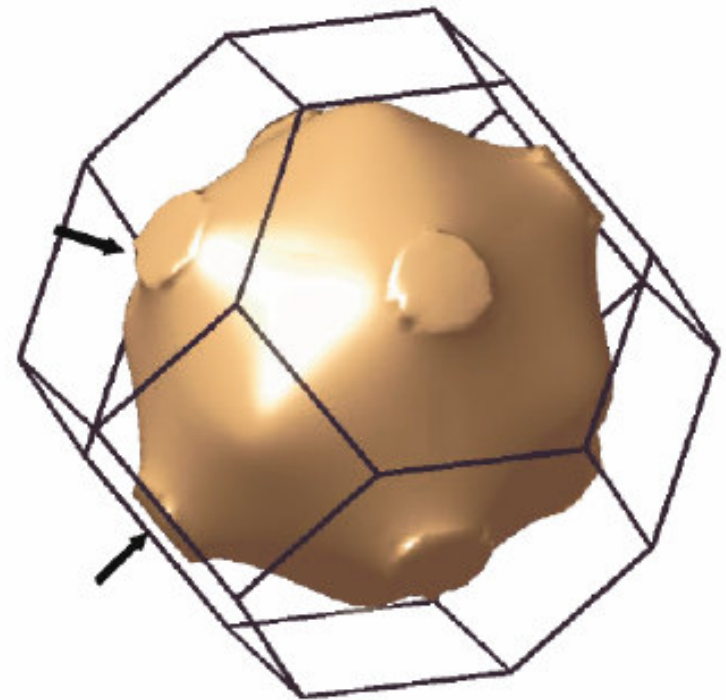


FIG. 1 (color). 3D plot of the FS of bcc Cu calculated by FLAPW (full-potential linearized augmented plane wave) calculations described in the text. The FS has twelve necks at the center of the $\{110\}$ Brillouin zone boundaries (N point). The neck marked by a red arrow and the two necks marked by black arrows correspond to the peaks in Fig. 4(a) (the anisotropy of the 2D-ACAR spectrum projected along the $[100]$ direction) marked by red and black arrows, respectively.

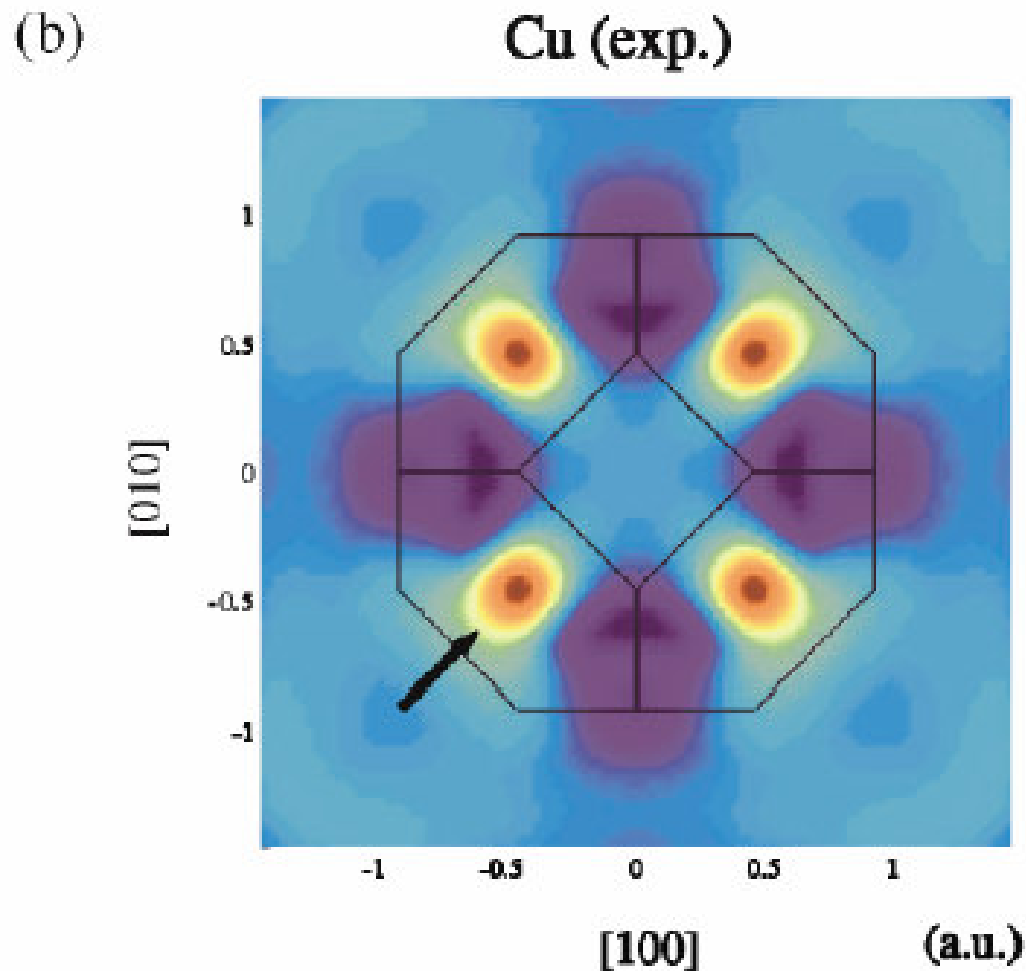


FIG. 2 (color). 3D plots of (a) the FS of bulk Cu (fcc structure) calculated by FLAPW calculations and (b) anisotropy of experimental 2D-ACAR projected along the $[100]$ direction. The four peaks in the plot of the anisotropy correspond to the eight necks at the center of the $\{111\}$ Brillouin zone boundaries (L point); the marked peak (arrow) in (b) arises from the two necks (arrows) in (a). The color scale is determined so that dark red and dark blue are assigned to the top of the peaks and the bottom of the valleys, respectively.

2D-ACAR谱仪

□ 探测器:

多探测器阵列: Brandeis大学 64NaI(Tl)

多丝正比室: 铅转换体

γ 位置灵敏探测器: Ge探测器, 多道板

Anger相机: 1958年提出, 一个大NaI晶体
对应几十个光电PMT

□ 角分辨:

$0.2*0.2 \text{ mrad}^2$

2D-ACAR种类

□ 多探测系统:

Berko: 64

Tsukuba Univ. 256 BGO

□ 多丝正比室:

Jeavons(CERN, Deneva Univ.) 10*10,

Mijnarends(荷兰)30*30cm MWPC

□ **Anger** 相机: 已商用

印度; 俄罗斯等

中国科学技术大学80年代研制成我国
第一台(唯一)一维角关联装置

- 日本筑波大学的**2D-ACAR**谱仪由二组各**128个BGO**闪烁体组成，每个都配有光电倍增管，总角分辨是**1.05mrad**，每个谱的计数要达到 8×10^6 个。由测量结果进行图象重组，可获得三维动量密度分布谱。
- 1997年日本**KEK**的**T.Kurihara**等人尝试用闪烁纤维作为位置灵敏探测器用于**2D-ACAR**研究，闪烁纤维的直径只有**6mm**，因而可获得图像分辨达**20线/mm**。

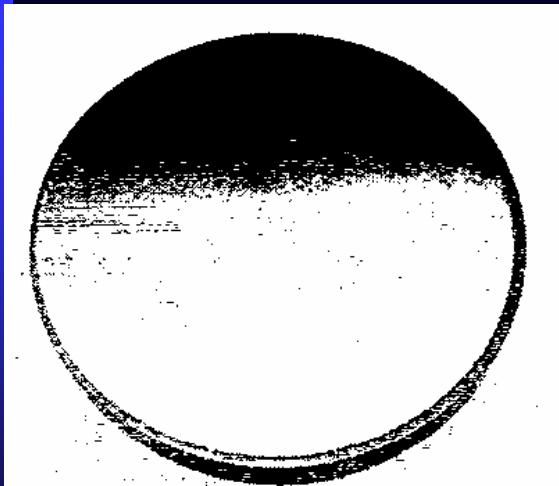
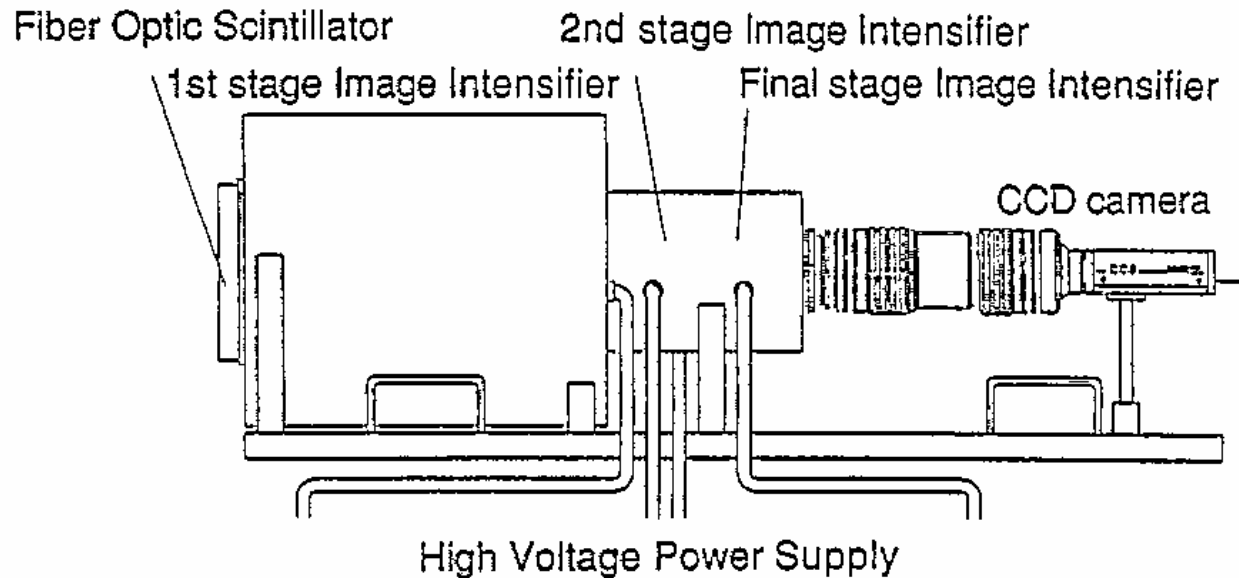


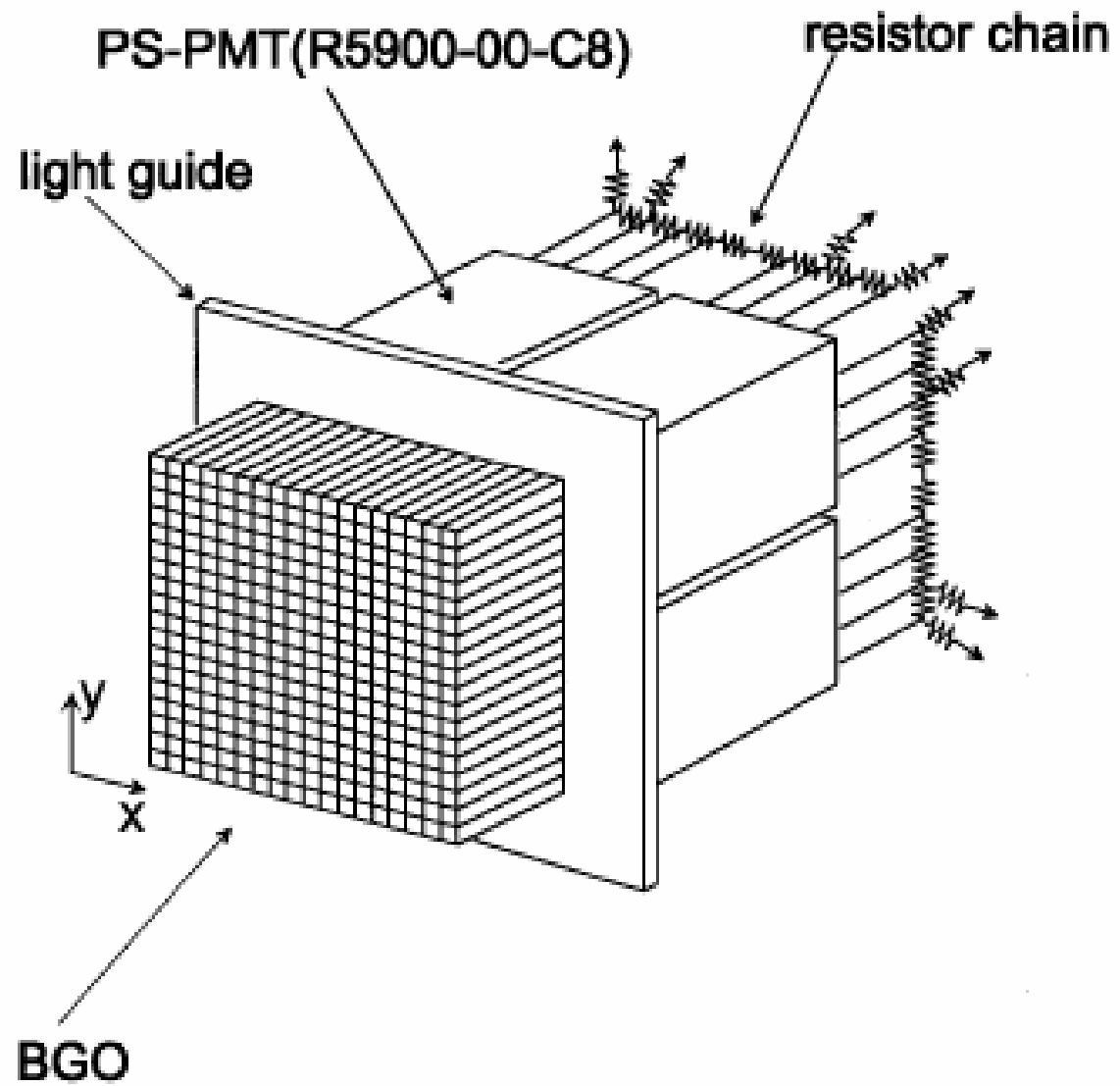
Fig. 1. Fiber-optic scintillator coupled to an image intensifier. One surface side is coated by aluminum for reflecting light. The size of this scintillator is 100 mm in diameter and 12.7 mm in thickness. A fiber diameter is 6 μm .

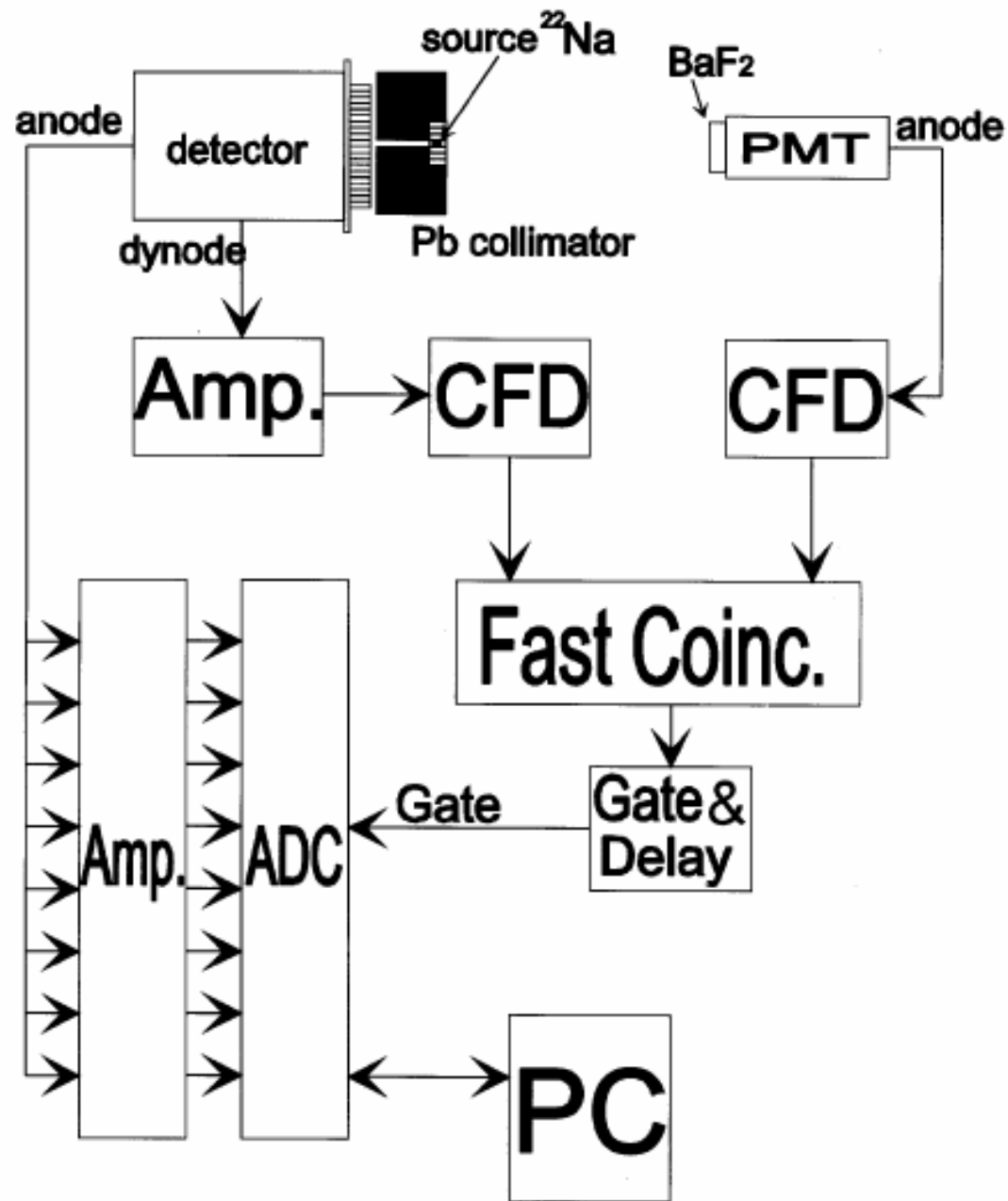


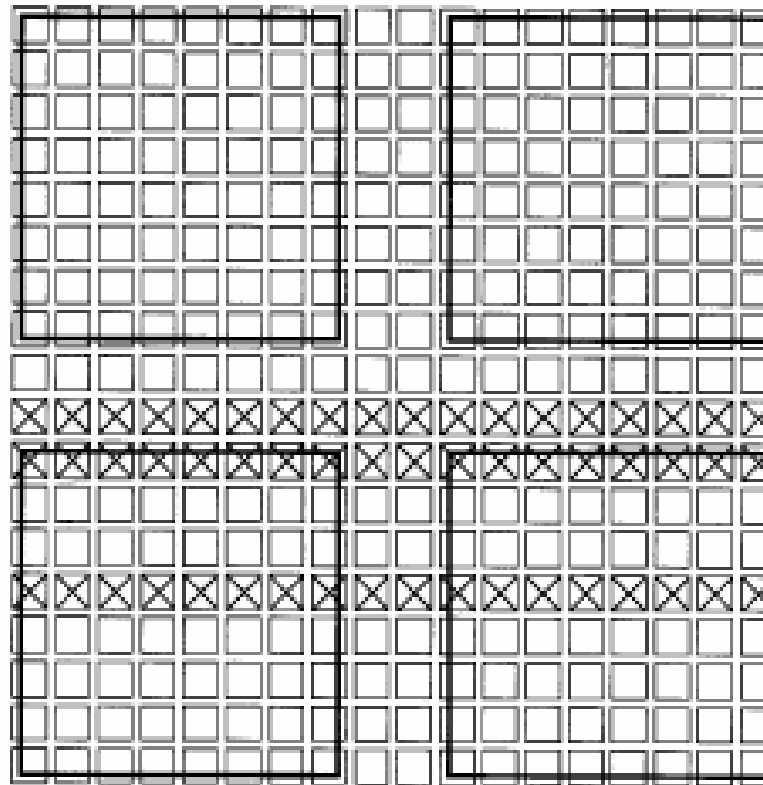
Detector system with a fiber-optic scintillator and an image intensifier.

Metal-package position-sensitive photomultiplier tubes

- A compact (28*28*20 mm) metal package PSPMT (R5900-00-C8) is now available from Hamamatsu Photonics Co. Ltd. .This PS-PMT has a sensitive area of 22*22 mm. The insensitive area of a closely packed array of these PS-PMTs is only 6 mm wide. By using a light guide between the scintillator array and the PS-PMT array, it may be possible to construct a large detector which has no dead area. In this work we constructed a prototype of such a position-sensitive γ -ray detector with four metal package PS-PMTs.







← row9

← row8

← row5

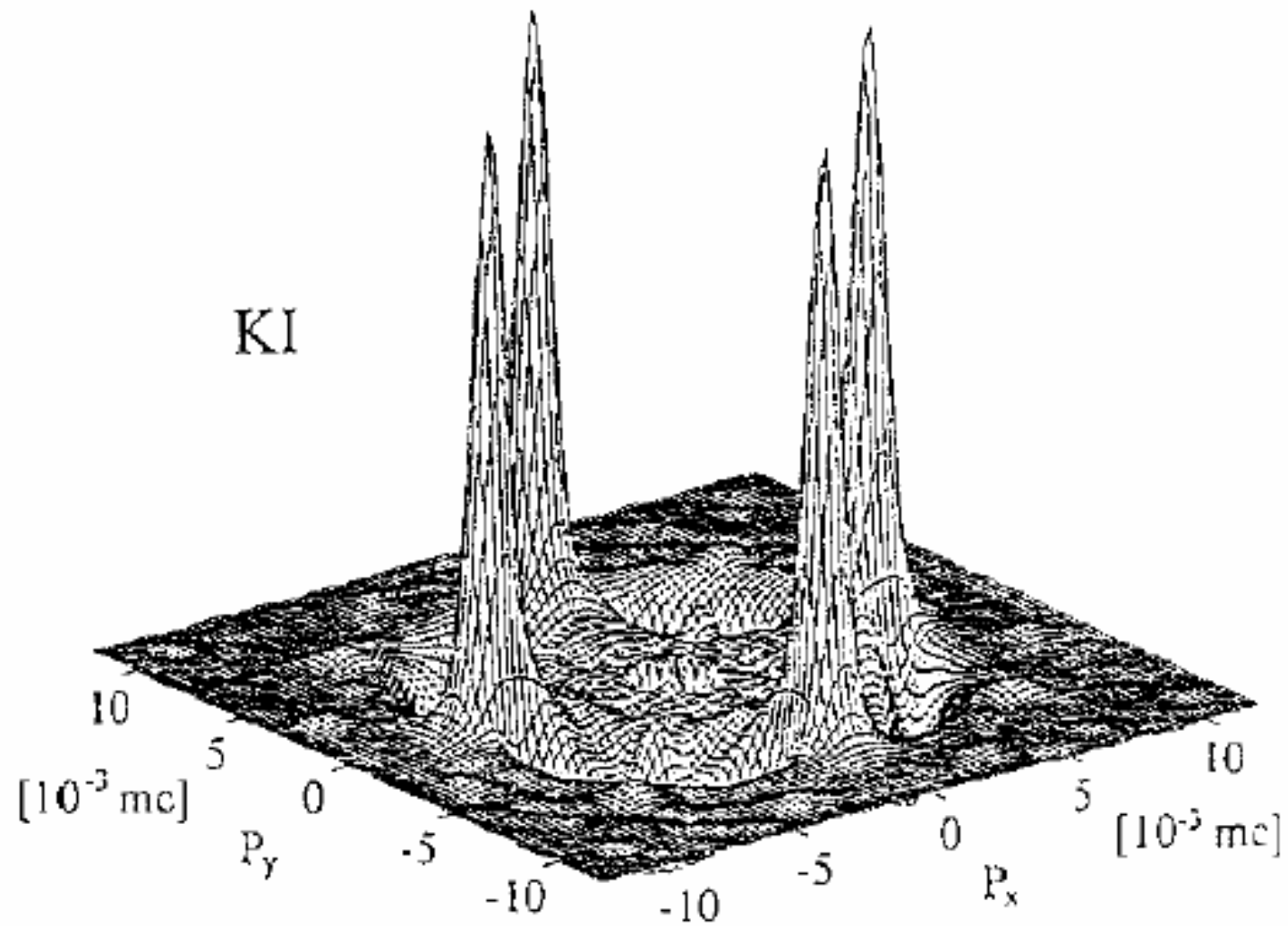


Fig.2. Anisotropy of 2D-ACAR for KI at 15K.

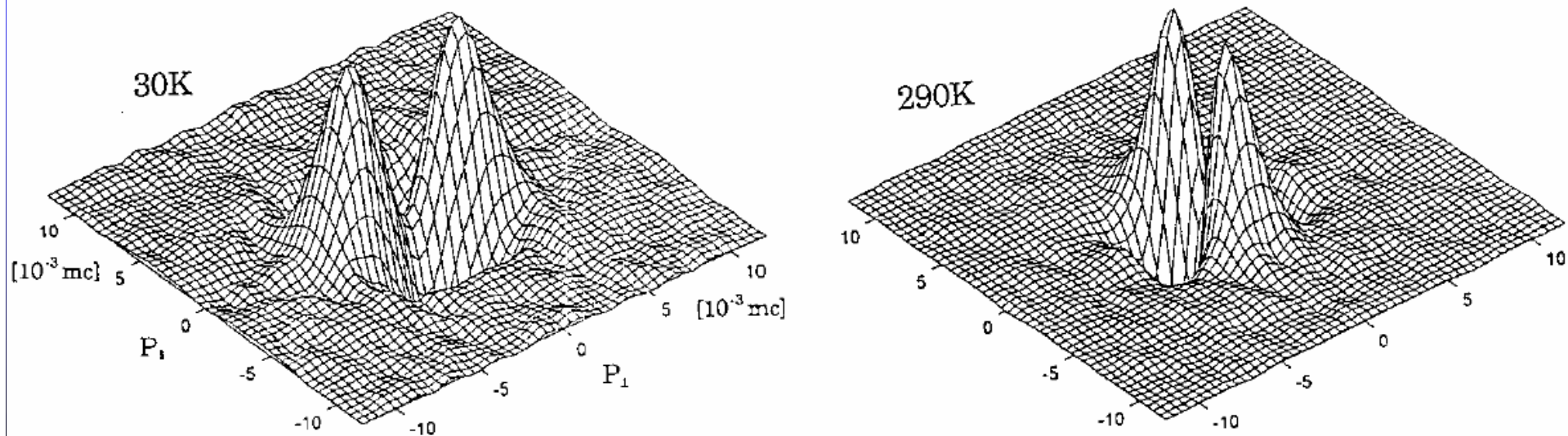
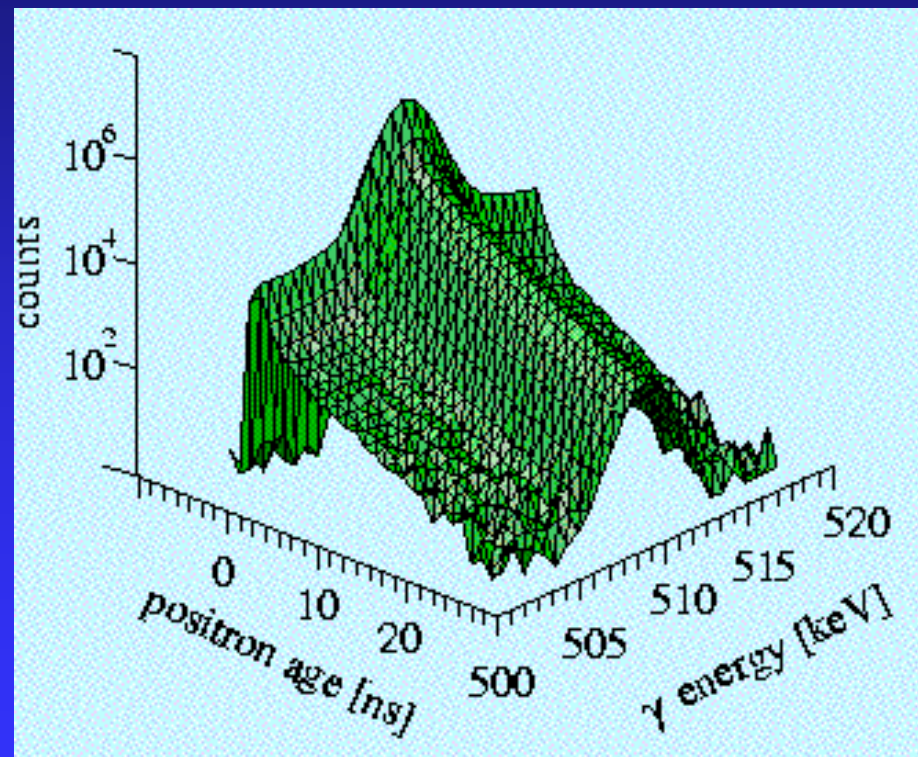


Fig.3. Anisotropy of 2D-ACAR for $[\text{Zn}(\text{ptz})_6](\text{BF}_4)_2$ at 30K and 290K.

6. AMOC技术



- ✿ 1975, Brummer等人首先在多普勒展宽测量引进寿命选择技术。
- ✿ 1978年, Maier和Myllyla重新建立了 $\beta^+ \gamma$ 测量技术, 他们认为, β^+ 探测器的探测效率通常为100%, 而使用触发 γ (1.27MeV) 作start信号的探测器其探测效率小于10%, 这样就可用更小的时间获得更好的统计。他们指出, 如果采用相对论正电子束就可不需使用能量过滤器, 因为接近光速的正电子穿过闪烁体时, 正电子的初始能量与能量损失已不重要。



- 1976年， MacKenzie和McKee首先提出寿命-动量关联(Age-Momentum Correlation)概念。
- 1992年， Stoll和Wesolowski等人第一次给出缩写AMOC。

Materials Science Forum Vols.105-110(1992)pp.1989-1992

$\beta+\gamma$ E Age-momentum-correlation measurements with an MeV positron beam

H.Stoll, P.wesolowski, M.Koch, K.maier, J. Major and A.Seeger

Max-Planck-institut fur metallforschung Institut fur Physik

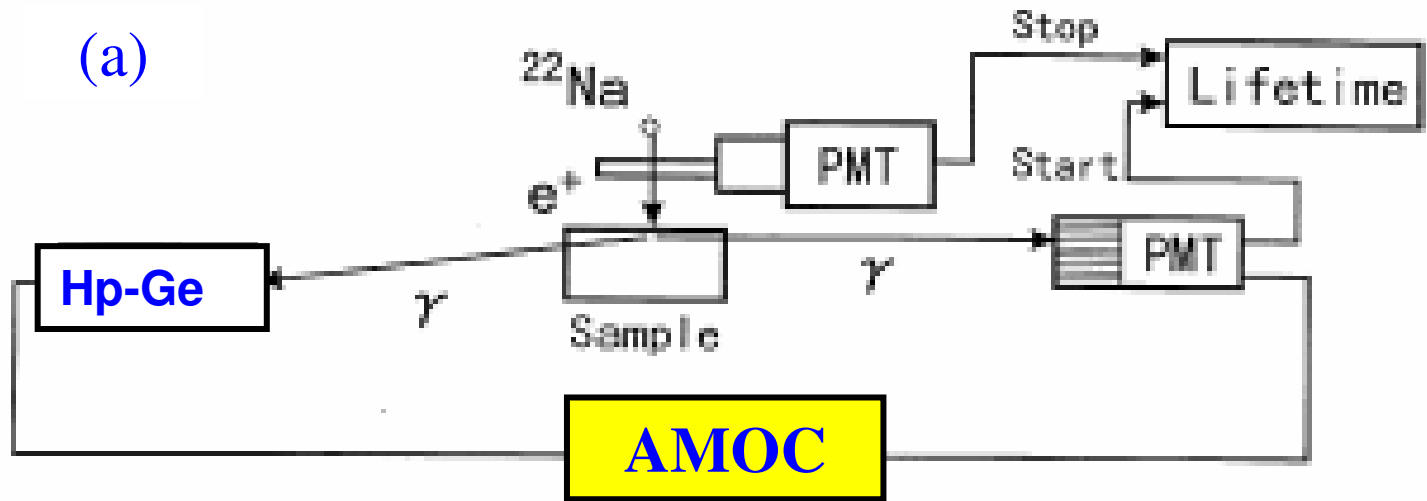


AMOC技术按测量寿命的起始触发信号分，主要有两种：

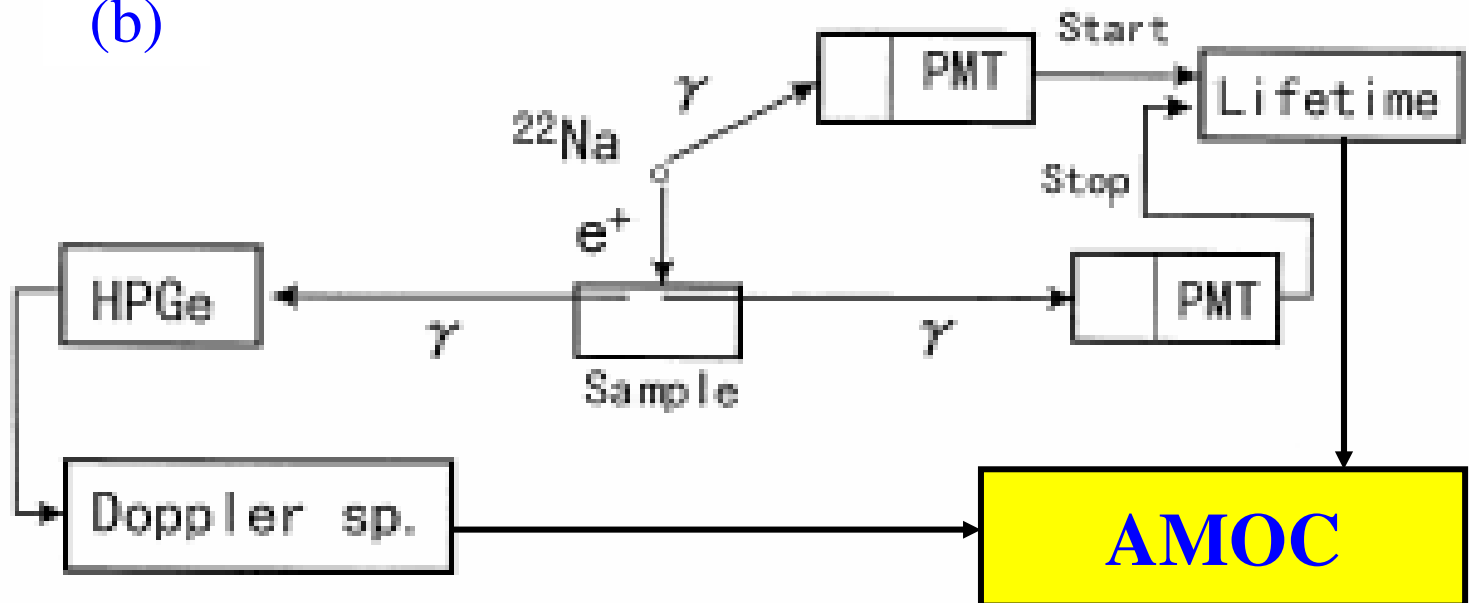
- 采用触发 γ (1.28MeV) 作起始信号，即所谓的AMOC- γ γ ΔE γ 技术；
- 采用正电子作起始信号，即AMOC- β^+ γ ΔE γ 技术。

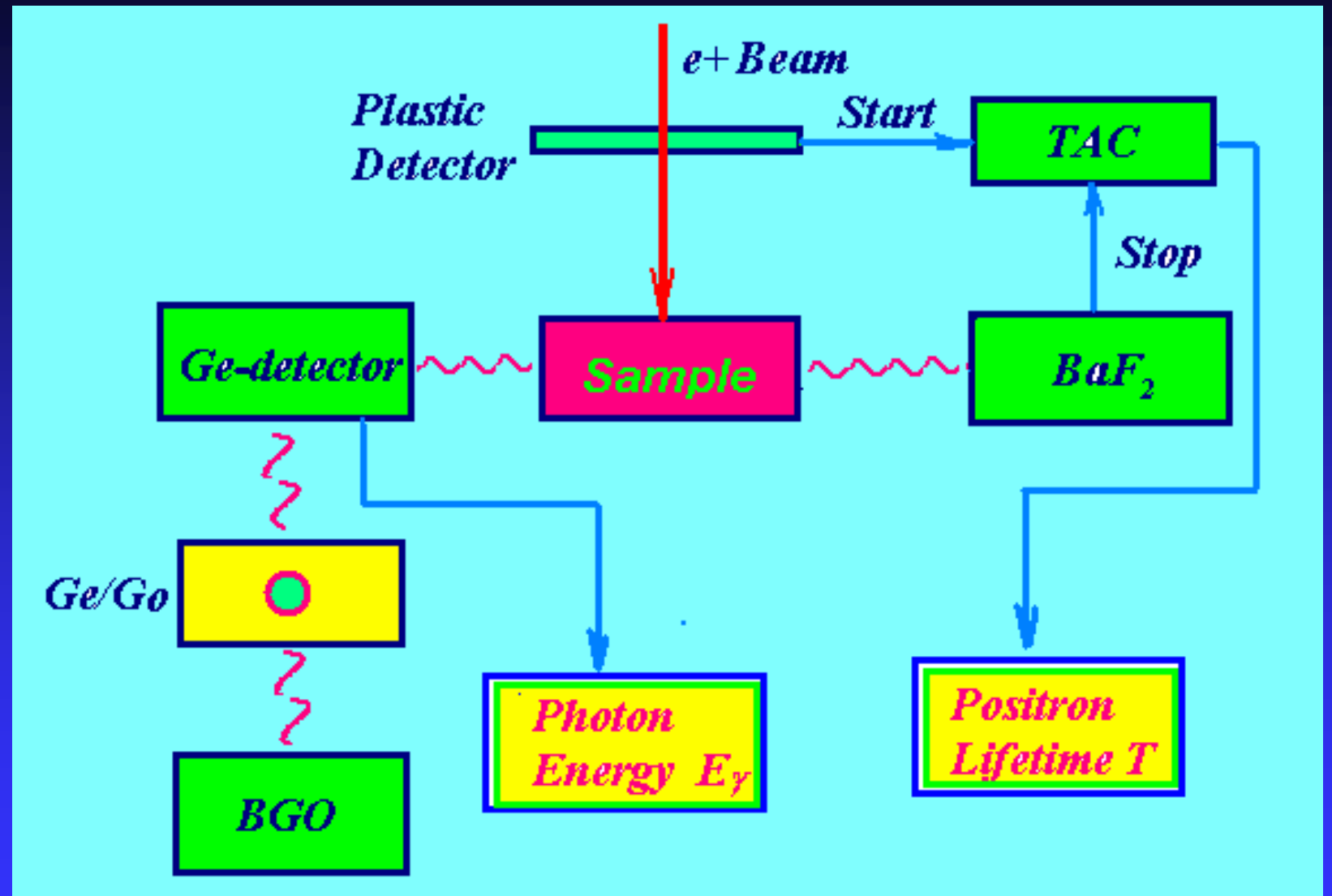


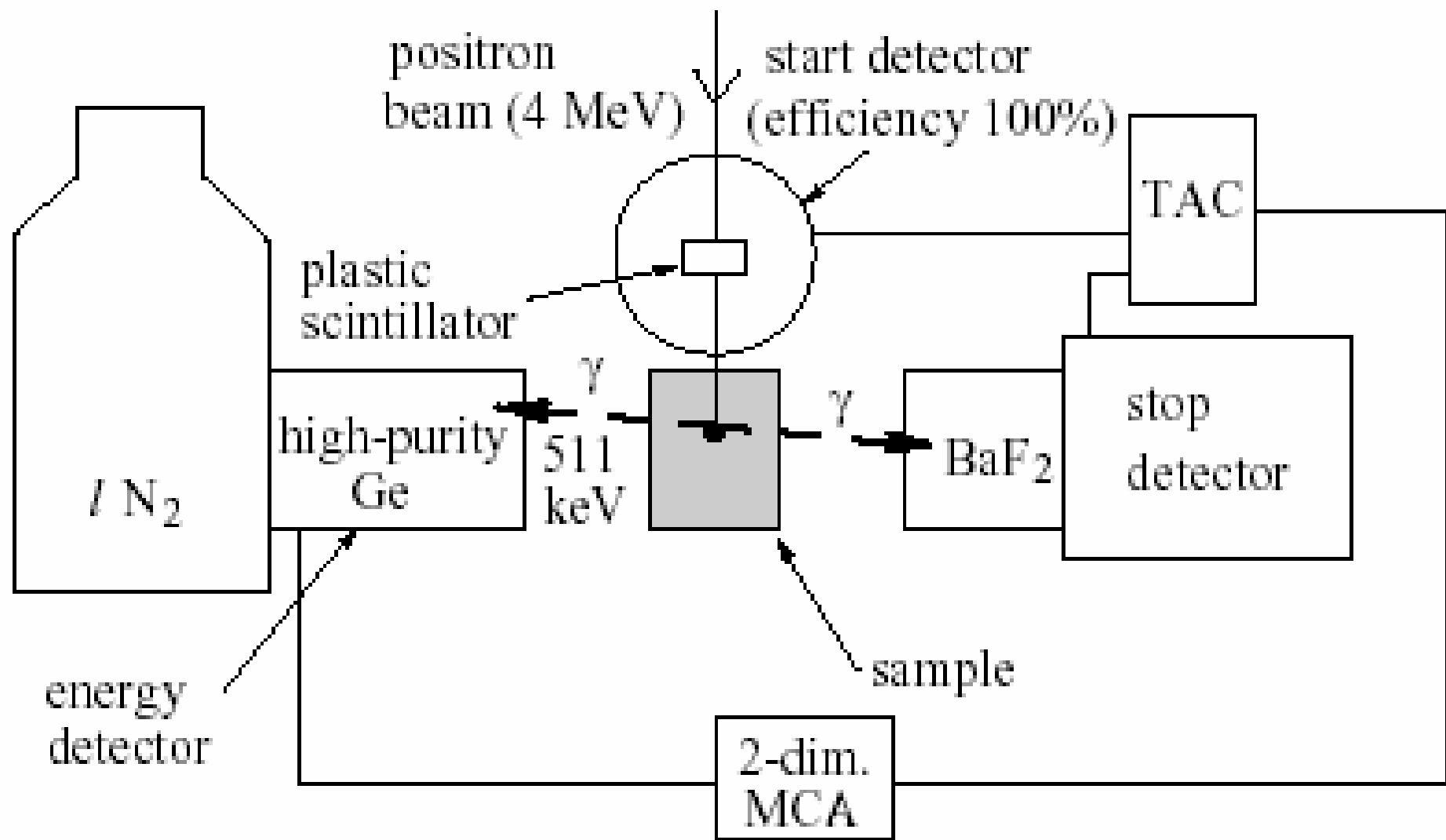
(a)

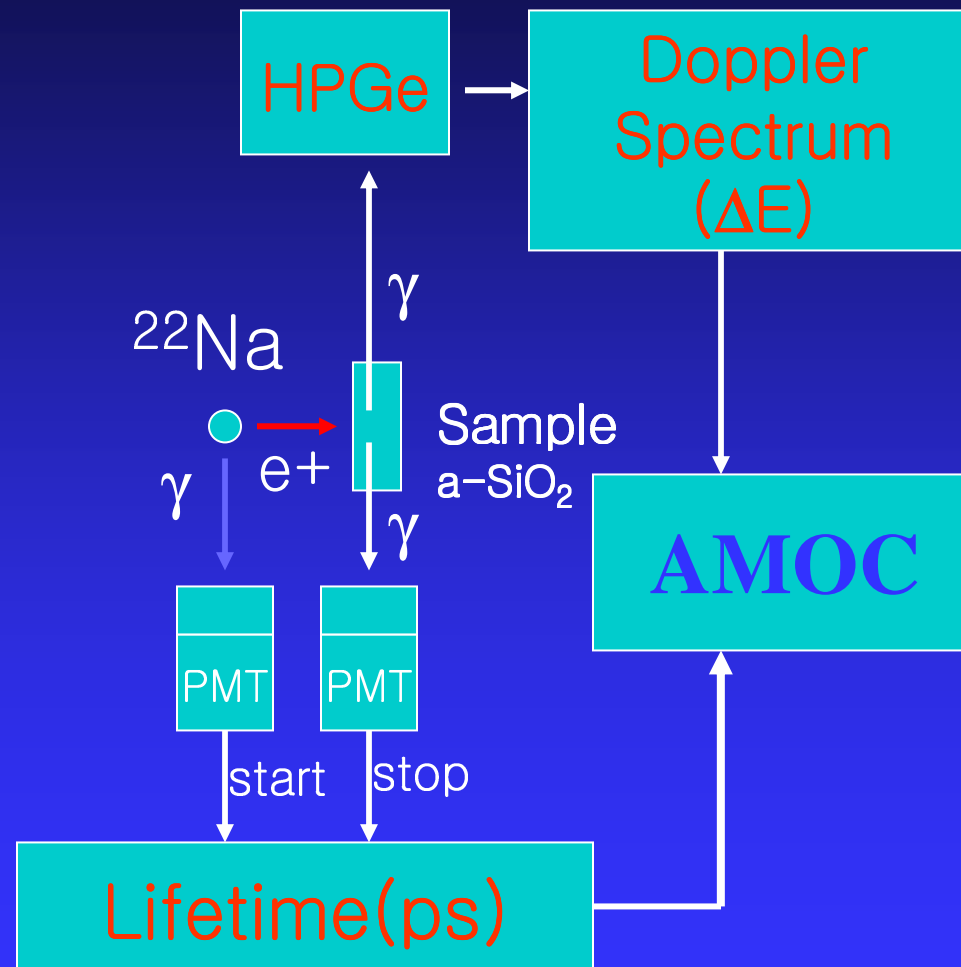


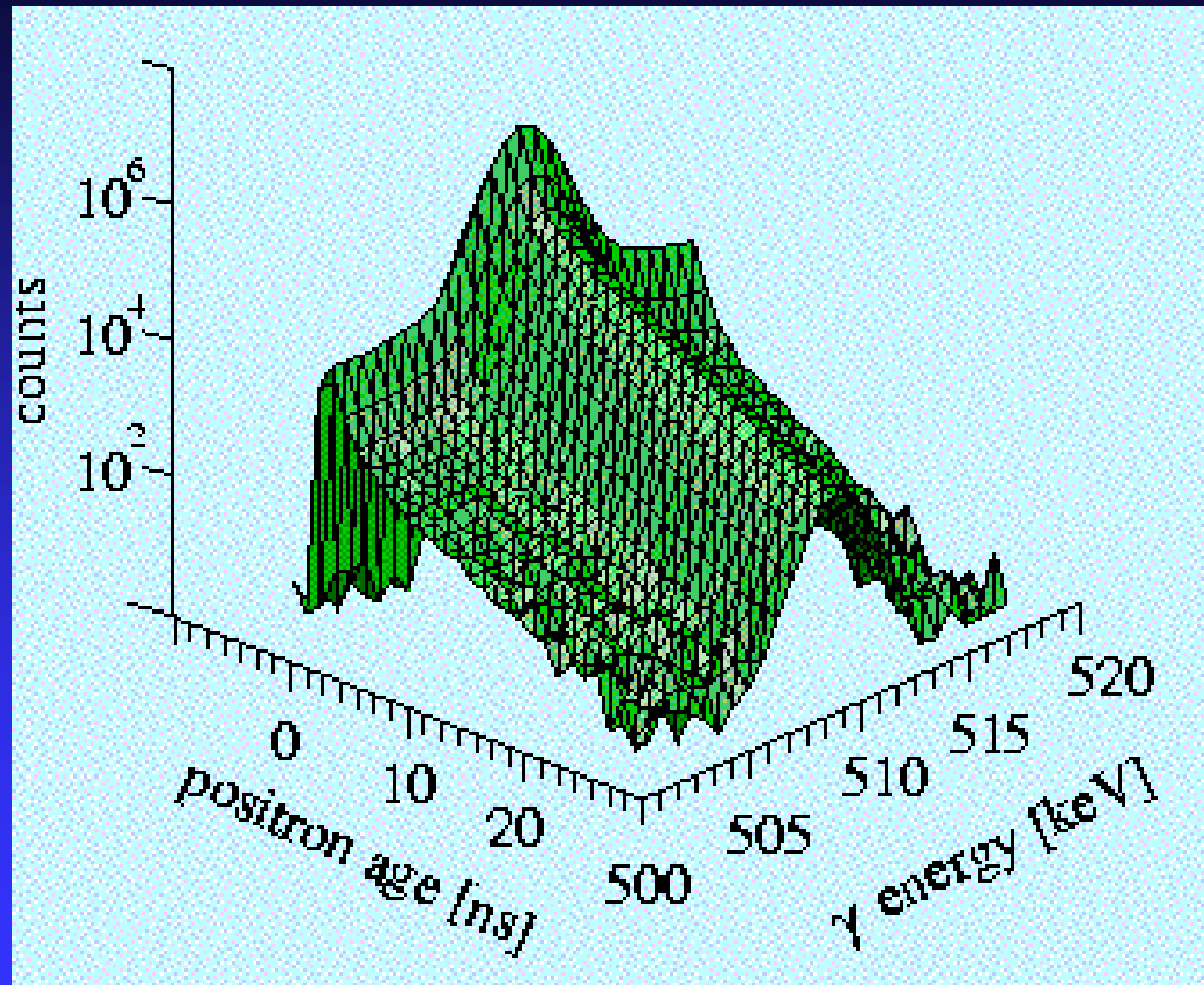
(b)











- * **J.Kostamovara**等人利用基于 $^{68}\text{Ge}/^{68}\text{Ga}$ 正电子源的AMOC- $\beta^+ \gamma \Delta E \gamma$ 技术研究了AI的各种参数。由于AMOC- $\beta^+ \gamma \Delta E \gamma$ 技术通常需要高能的正电子束流，因而实验就受到限制；
- * **P.Wesolowski**等人利用基于加速器的正电子束建立了AMOC- $\beta^+ \gamma \Delta E \gamma$ 测量技术。
- * 德国Stuttgart的 **H.Stoll**小组在AMOC- $\beta^+ \gamma \Delta E \gamma$ 技术发展最具出色，他们专门建立了一个4MeV的正电子束流，开展了大量的工作。



AMOC探测系统研制



日本探测系统

Age-momentum correlation study of positronium, fine particle surface and monovacancy formation energy

T. Hyodo^{a,*}, N. Suzuki^b, H. Saito^a, Y. Nagai^c

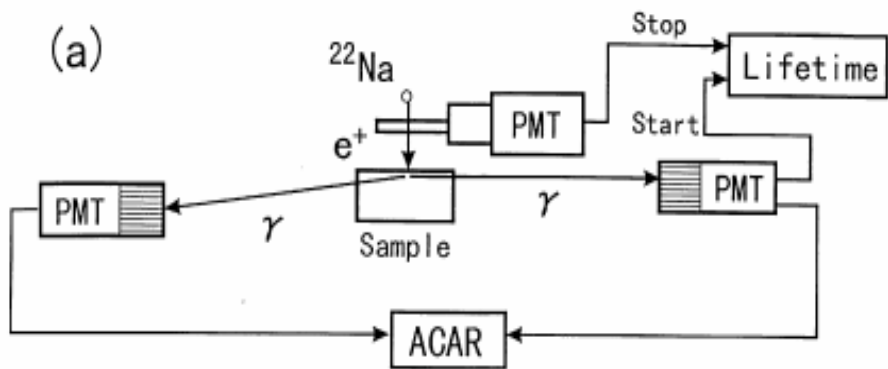
^a*Department of Basic Science, Graduate School of Arts and Sciences, University of Tokyo, 3-8-1 Komaba, Meguro-ku, Tokyo 153-8902, Japan*

^b*The Institute of Physical and Chemical Research (RIKEN), Hirosawa 2-1, Wako, Saitama 351-0106, Japan*

^c*The Oarai Branch, Institute for Materials Research, Tohoku University, Oarai, Ibaraki 311-1313, Japan*

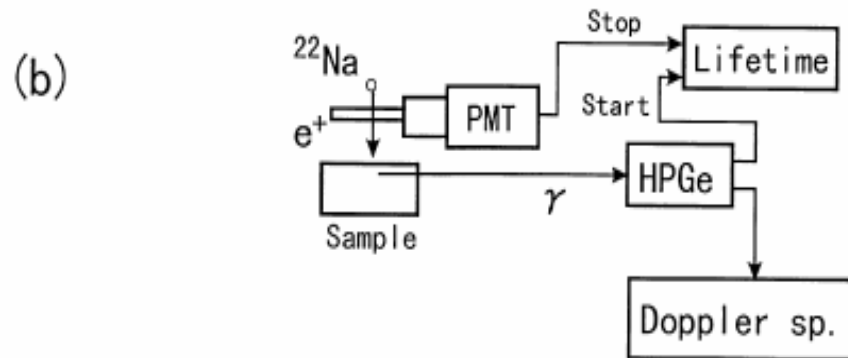
Radiation Physics and Chemistry 58 (2000) 767–769





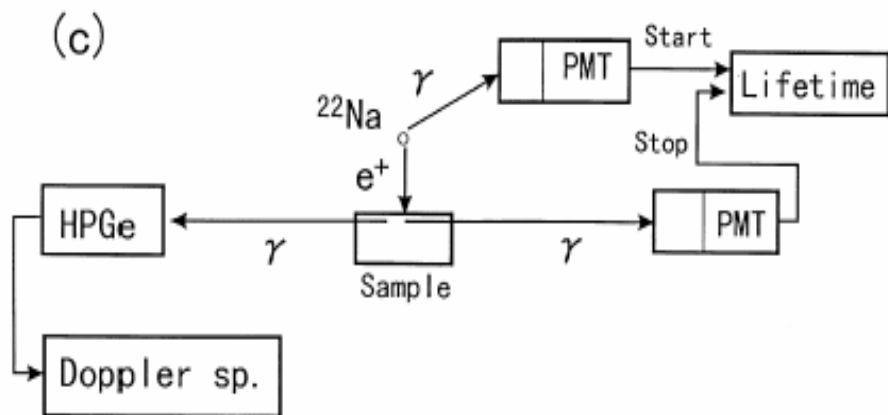
动量分辨: $1.3 \times 10^{-3} \text{ mc}$

时间分辨: 2.7 ns



动量分辨: $4.3 \times 10^{-3} \text{ mc}$

时间分辨: 4.8 ns



动量分辨: $4.3 \times 10^{-3} \text{ mc}$

时间分辨: 220 ps




Materials Science Forum Vols. 363-365 (2001) pp. 661-663
© 2001 Trans Tech Publications, Switzerland

Development of High-Rate Age-Momentum Correlation System with a Variable-Energy Pulsed Positron Beam

R. Suzuki¹, T. Ohdaira¹, T. Mikado¹ and G. Venugopal Rao²

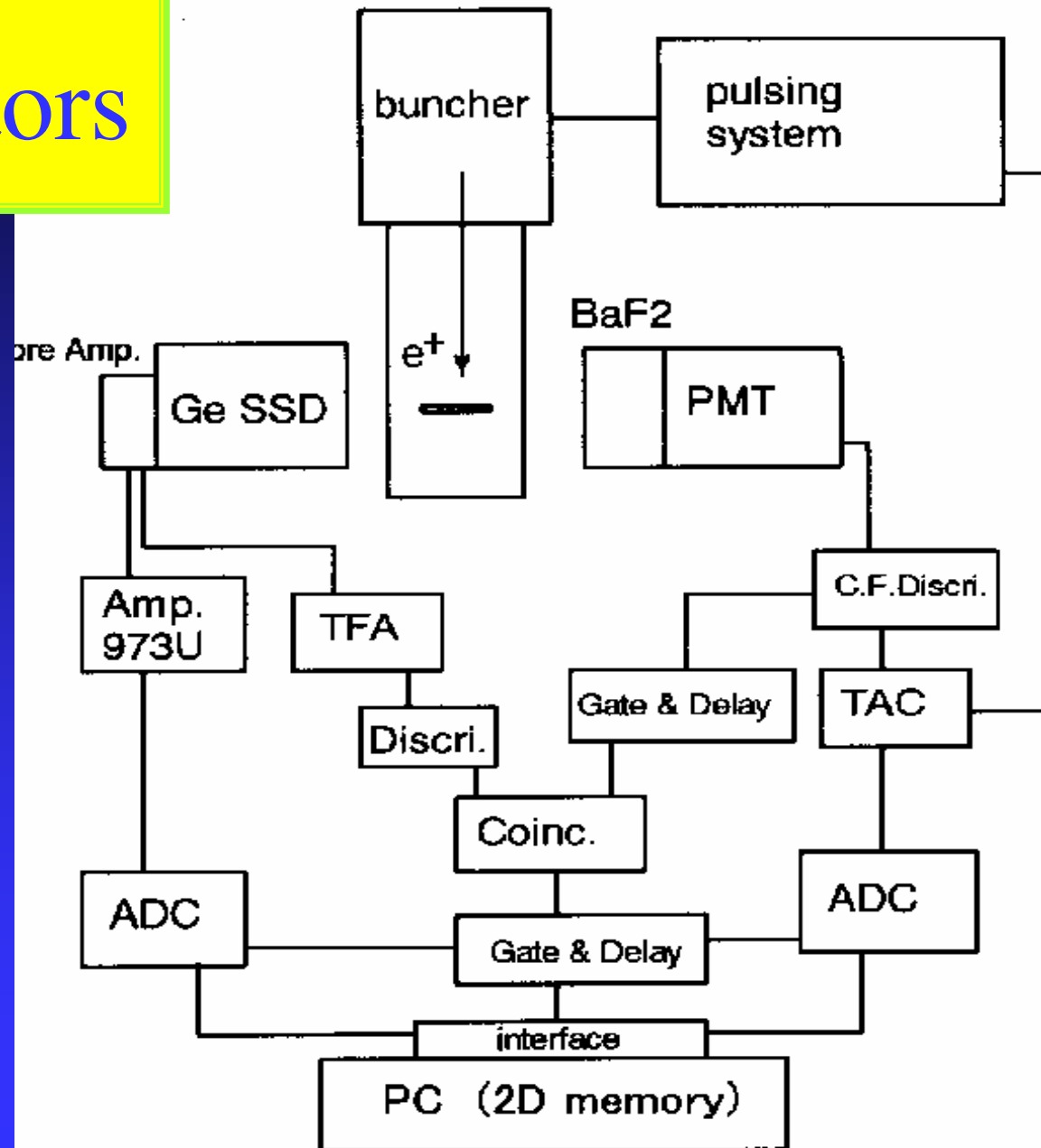
¹ Electrotechnical Laboratory, 1-1-4 Umezono, Tsukuba, Ibaraki 305-8568, Japan

² Indira Gandhi Centre for Atomic Research, Kalpakkam 603 102, India

The pulse-stretched beam is then short-pulsed to ~150 ps by a pulsing system developed for positron lifetime measurements [5]. The positron energy is variable from 0.3 keV to 25 keV, and the pulse interval is variable from 26 ns to infinity with 26 ns  step.



Detectors



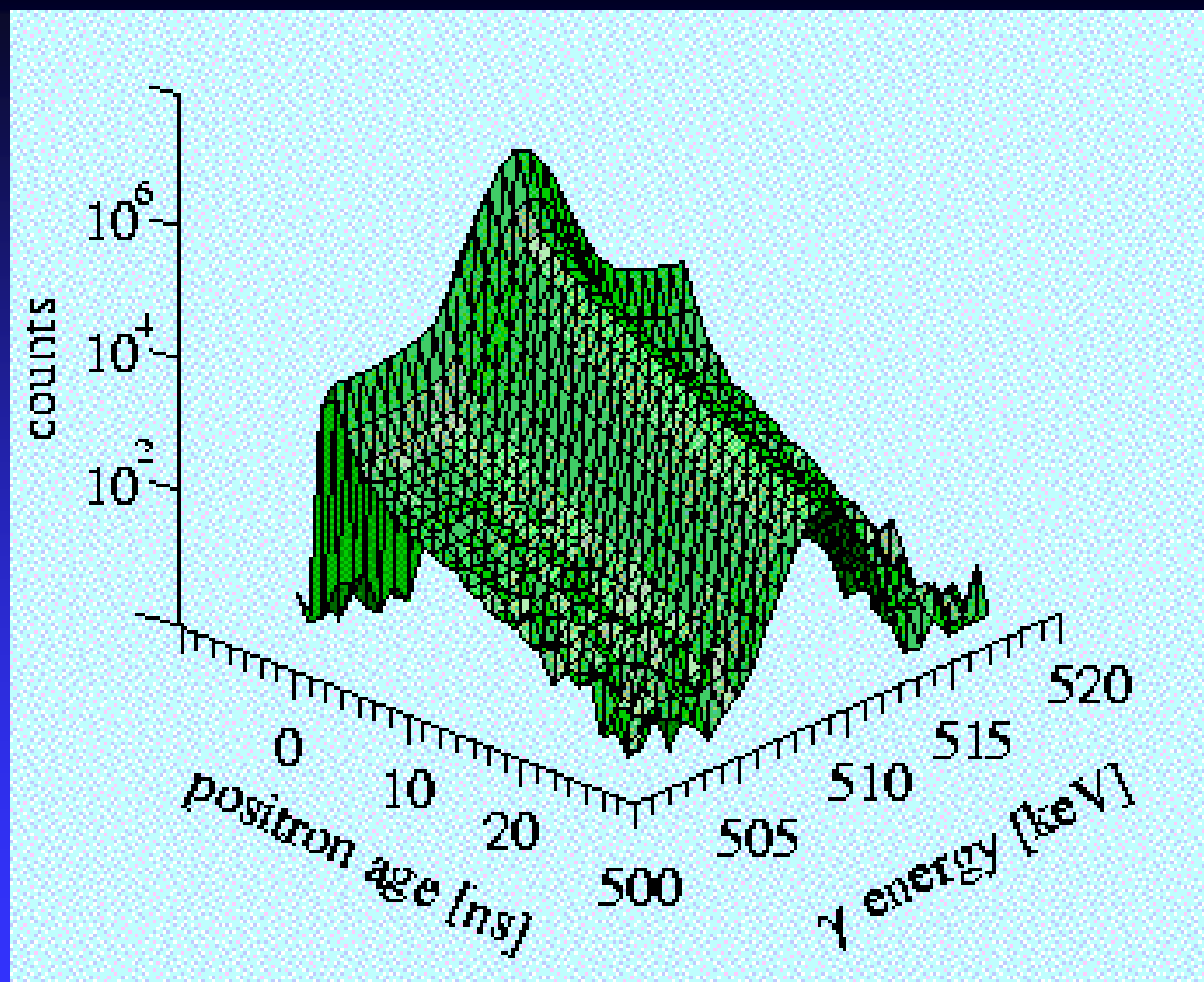
Detector

Detector one: $\Phi 50 \times 20\text{mm}$ BaF₂,
Hamamatsu R2083Q

Detector two: Ge SSD, +preamp+ Ortec973U

Coincidence count rate: $\sim 2000\text{cps}$





美国探测系统

COMBINED LIFETIME-MOMENTUM MEASUREMENT OF ORTHO-POSITRONIUM IN POLYMERS

M.Y. Ruan, W. Zheng* and J.D. McGervey

Department of Physics, Case Western Reserve University
Cleveland, OH 44106, USA

Materials Science Forum Vols. 105-110 (1992) pp. 1695-1698
Copyright Trans Tech Publications, Switzerland



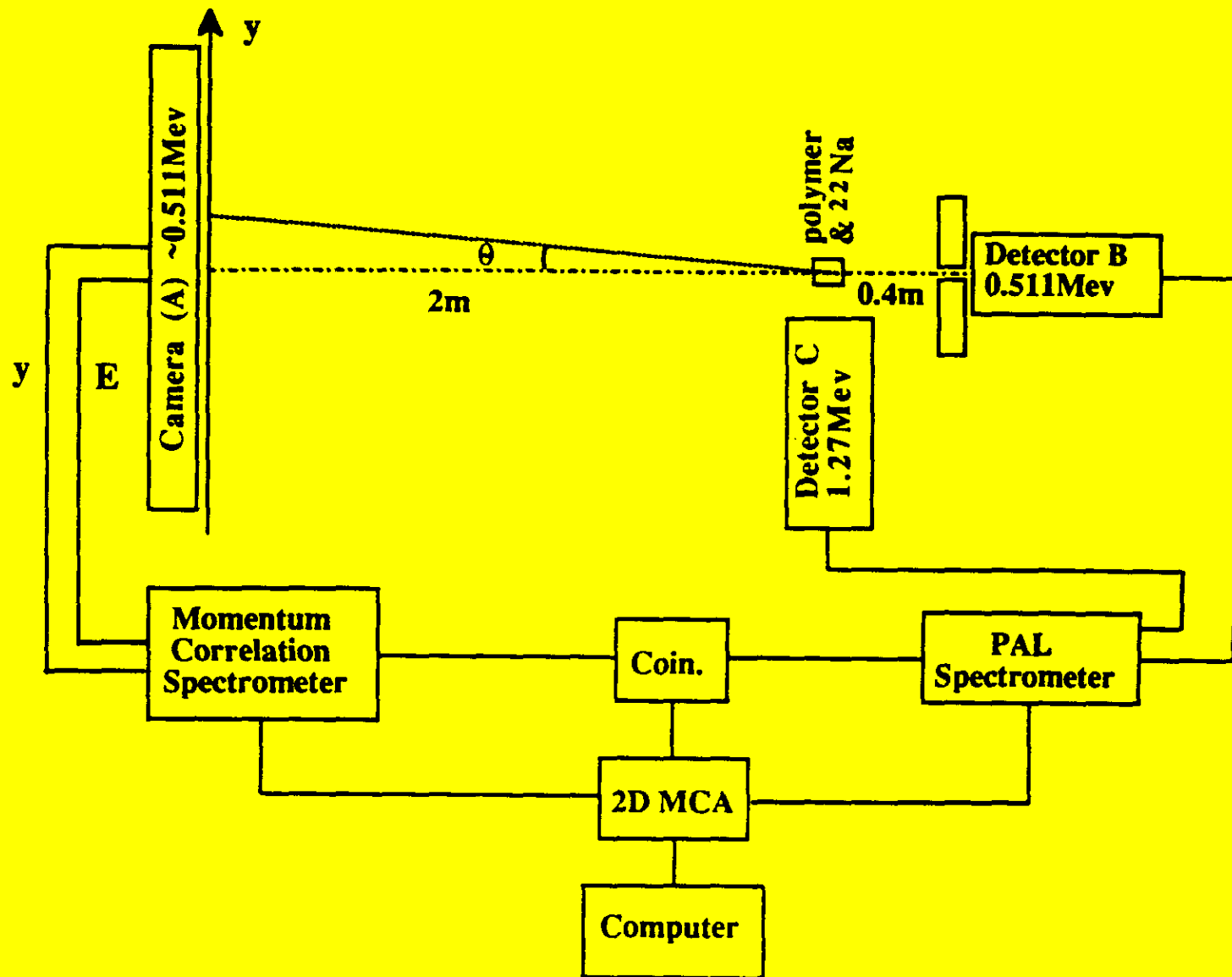


Fig. 1 Positron Annihilation Lifetime and Momentum Correlation System



Performances

- Time resolution 280ps
- Angles range: -13.2 mrd to 13.2 mrd
- Angle resolution: 2.8mrd
- Counting rate: 150/s for 60 μ Ci ^{22}Na



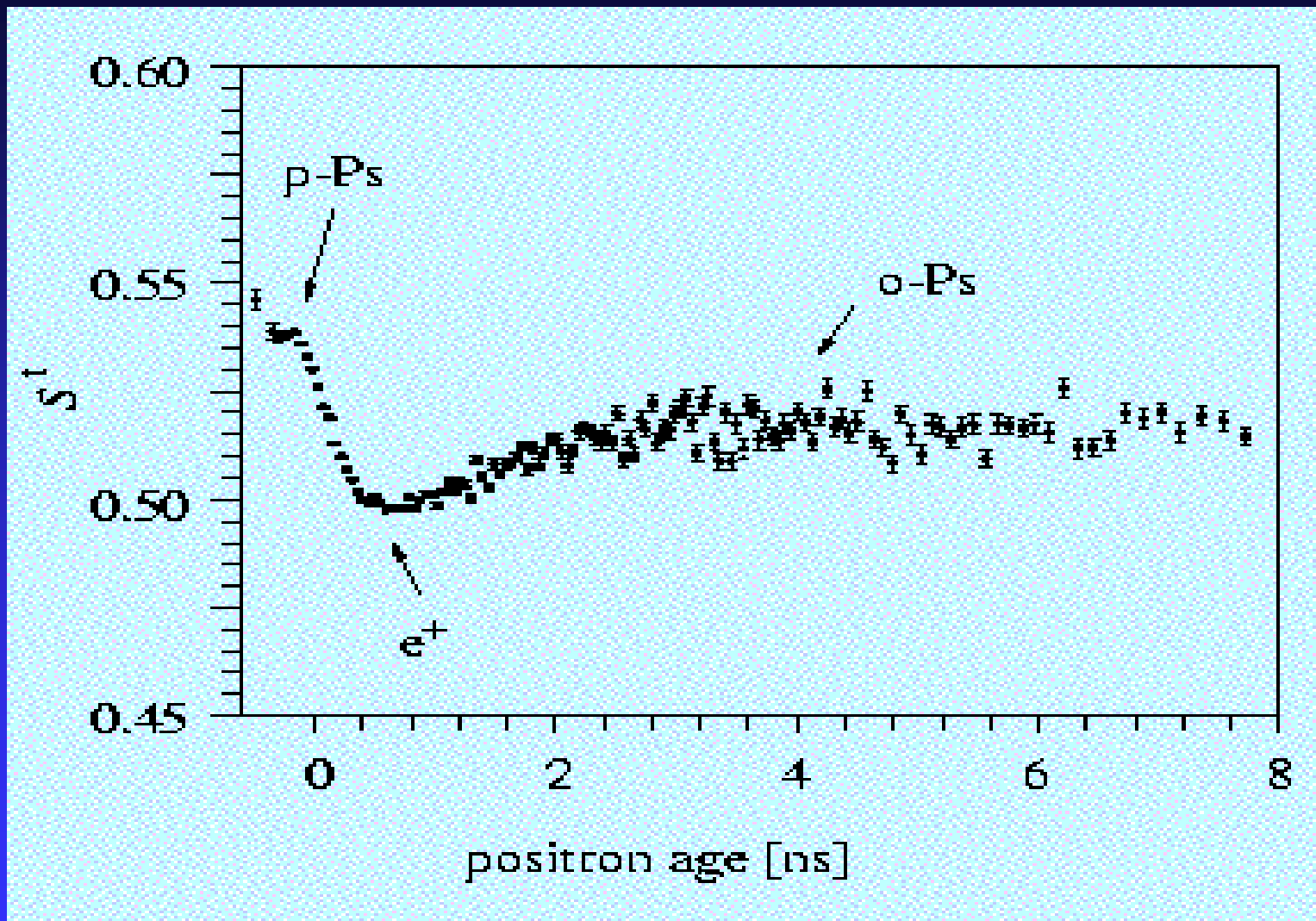
AMOC分析技术

S_t 分析技术

- ◎ AMOC二维谱是正电子湮灭时间和湮灭光子的多普勒展宽的关联。通常的正电子寿命谱可对所有正电子能谱积分得到，通常的多普勒展宽可对不同的寿命积分得到。
- ◎ 此外，还可以获得多普勒展宽的S参数随寿命的变化（即计算不同寿命下的S参数）称 S_t 线性函数：

$$S^t(t) = \frac{\int_{\pm\Delta p} N(p,t)dp}{\int N(p,t)dp} = \frac{\int_{\pm\Delta p} N(p,t)dp}{L(t)}$$

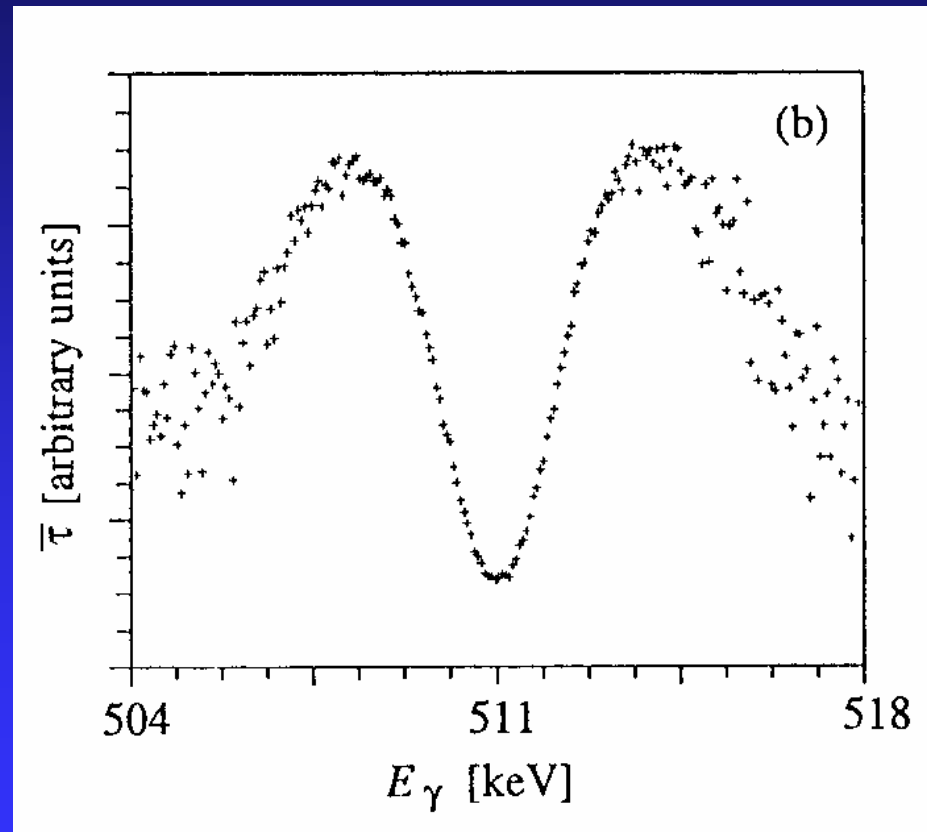




Tsukuba分析

从AMOC二维谱中抽取正电子平均寿命随正电子的能量变化的变化称Tsukuba（筑波）分析

平均寿命是以511keV对称分布的，在511keV处是一个谷。





二维分析

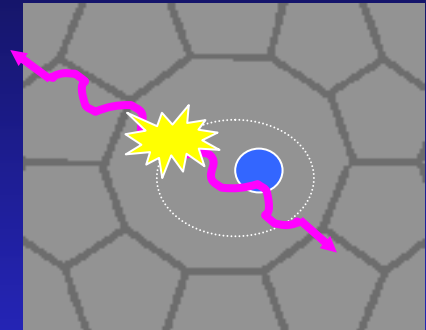
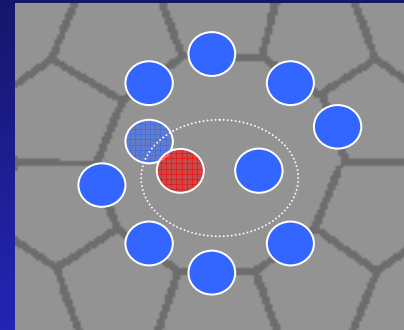
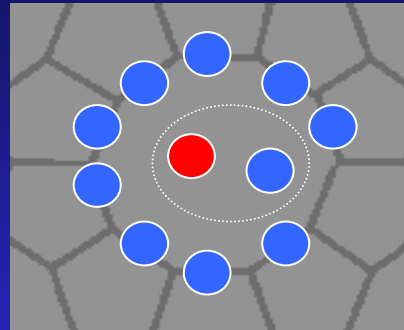
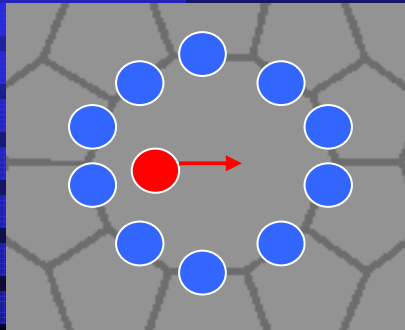
- * 要建立真正的二维AMOC分析技术，需要找到合适的模型，建立计数率 $N(p, t)$ 随时间 t 和能量变化的方程。结合初始条件，样品条件和仪器时间和能量分辨函数来获得理论解。这种分析技术目前国际上尚未建立。这是一个较复杂的分析过程，需要引进拟合参数和以及部分比例来获得更精确的信息，预计这种分析技术将包含下列因素：
 - 所有正电子态的多谱勒展宽线性参数和湮灭率。
 - 正电子态之间的跃迁率。
 - 正电子形成正电子偶素分量。
 - 谱仪的时间分辨函数和多普勒展宽分辨函数。
 - 实验本底。

正电子凝聚态物质中的湮没

O-Ps在凝聚态物质中的湮没主要有以下几种形式：

- pick-off 湮没
- 正-仲转换
- 磁猝灭
- 化学猝灭

“picked off” annihilation



e^+ thermalizes within tens of ps; e^+ preferentially locates in channels and cavities

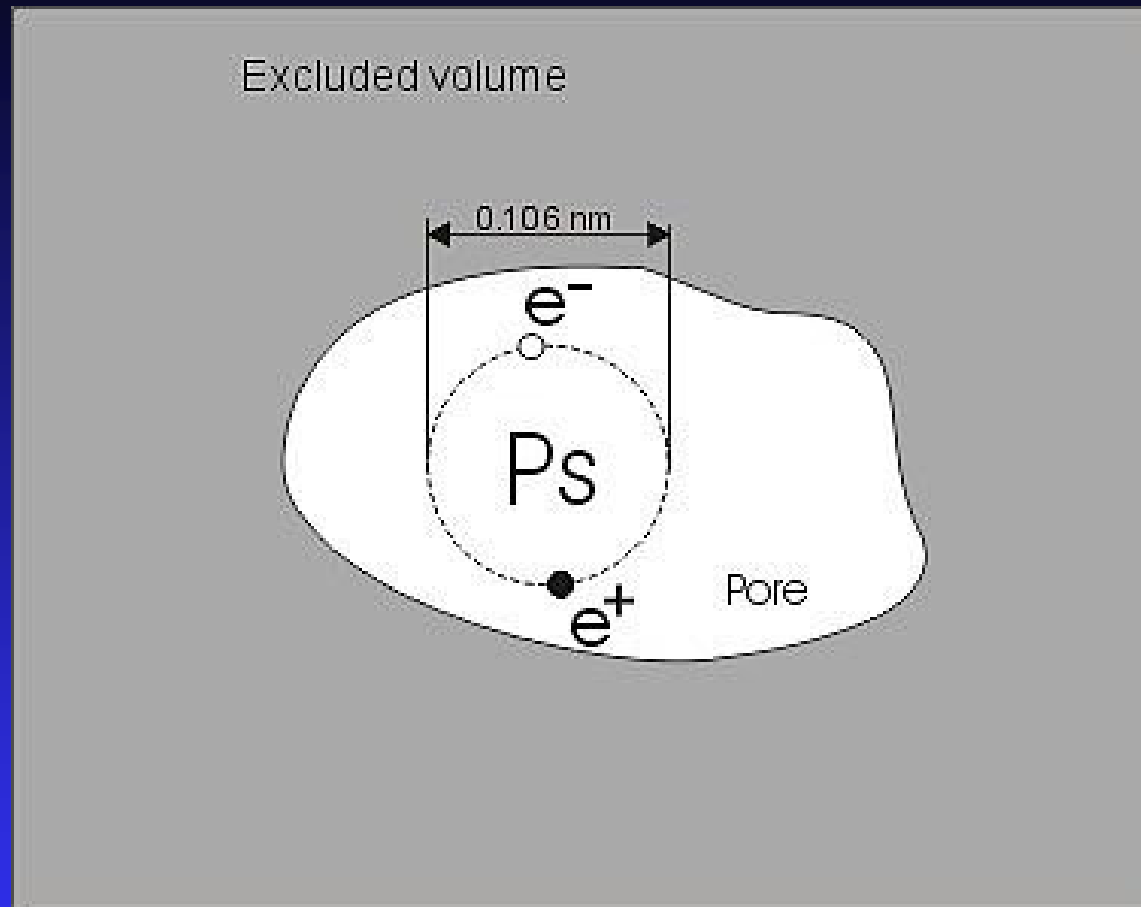
e^+ selects electron of solid and forms Ps with natural lifetime of 125 ps (para) or 140 ns (ortho)

e^+ in Ps is “picked off” prematurely by another electron of solid.

two gamma rays with characteristic energy of 511 keV are emitted.

Ps在凝聚态物质中的几种 “撞击”湮没模型

- Infinite spherical model (T-E关系式)
- ETLT(Elastic Thermalization Lifetime analysis)
- Bubble Model (in liquid)



Ps is preferentially localized in pore before the annihilation occurs.

Tao-Eldrup Model

- The annihilation rate is proportional to the overlapping the o-Ps wave function with the environment as it was postulated by **Tao 1972** and put into shape by **Eldrup et al. 1981**. In the case of spherical cave of radius R it can be expressed as follows:

$$\lambda_{pick-off} = \lambda_b \int_R^{R+\Delta} \psi_+(r) r^2 dr$$

- It is also common assumption that the Ps has no internal structure than the wave function above is proportional to the zero-order spherical Bessel function: $\Psi_+(r) = \text{const } J_0(r)$. The Ps wave function penetrates the environment at the depth Δ . From (2) one can obtain the well known Tao-Eldrup equation which allows to establish the direct relation between the lifetime of o-Ps with the radius of the spherical cave:

$$\lambda_p = 2 \left[\frac{\Delta R}{R + \Delta R} + \frac{1}{2\pi} \sin \left(2\pi \frac{R}{R + \Delta R} \right) \right].$$

The total *o*-Ps decay rate λ_{o-Ps} is given by

$$\lambda_{o-Ps} = \lambda_p + \eta\lambda_3,$$

where $\lambda_3 = \frac{1}{142} \text{ ns}^{-1}$ is the *o*-Ps decay rate in a vacuum and $\eta = |\psi(0)|^2 / |\psi(0)|_{\text{vacuum}}^2$ is the relative contact density,

J. Phys. Chem. B 2001, 105, 4657–4662

4657

Determination of Pore Size in Mesoporous Thin Films from the Annihilation Lifetime of Positronium

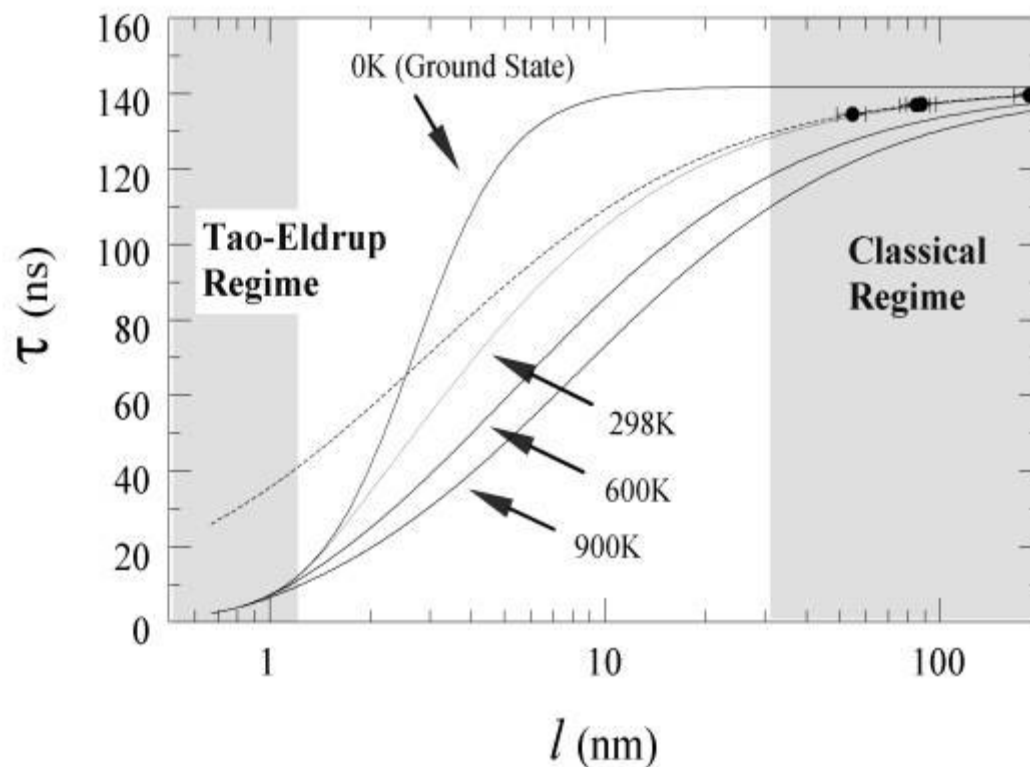
T. L. Dull, W. E. Frieze, and D. W. Gidley*

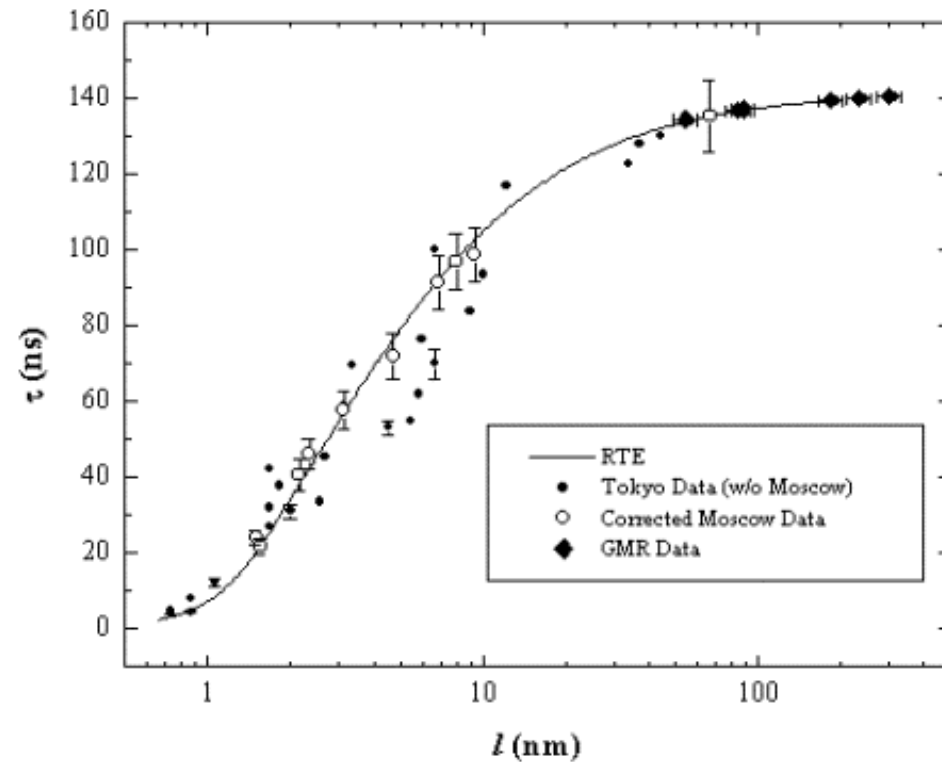
Department of Physics, University of Michigan, Ann Arbor, Michigan 48109

J. N. Sun and A. F. Yee

Department of Materials Science and Engineering, University of Michigan, Ann Arbor, MI

Received: November 14, 2000; In Final Form: February 15, 2001





A comparison of the RTE model with experimental data acquired in bulk materials.

AMOC技术的应用

冷凝稀有气体中的Ps态

A.Siegle用AMOC研究液态和固态Ne, Ar和Kr。固态Ar在16k时, o-Ps寿命为2.4ns。固态Kr在50k时o-Ps寿命为2.1ns。这可用o-Ps的pick-off湮灭来解释, 在液体中, 更长的o-Ps寿命可用o-Ps在长寿命自局域态的自湮灭, 即所谓的Ps气泡来解释。如在固态Ne中, o-Ps的寿命在15k时为5.3ns表明Ne中同样有Ps气泡形成。



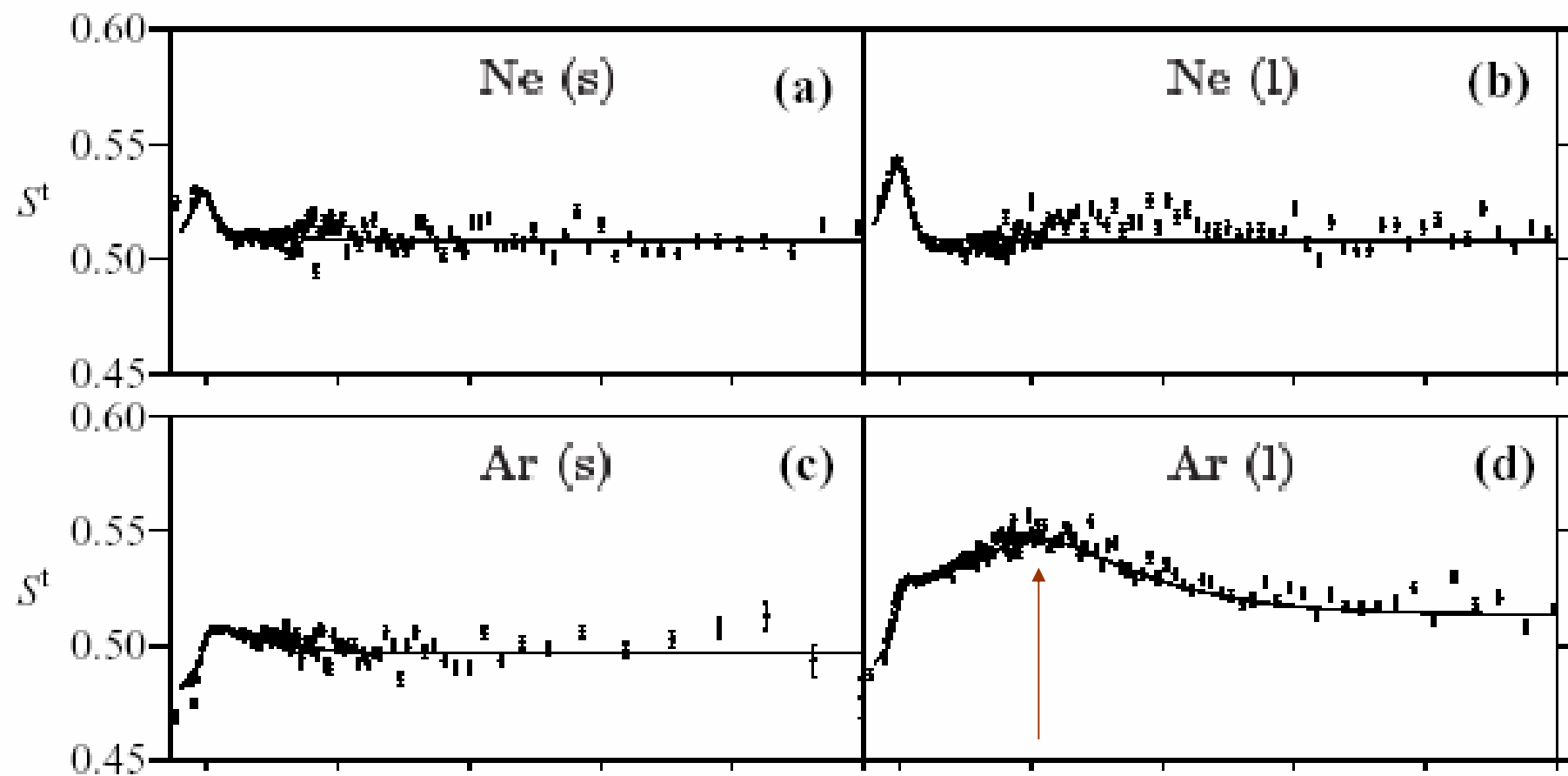


Fig. 8: Lineshape functions $S^t(t)$ calculated from AMOC data and model functions (solid lines) for condensed rare gases: Solid Ne at 15.2 K (a), liquid Ne at 26.0 K (b), solid Ar at 83.3 K (c), liquid Ar at 86.3 K (d), solid Kr at 50.0 K (e), liquid Kr at 120.0 K (f), solid Xe at 150 K (g), and liquid Xe at 163 K (h).

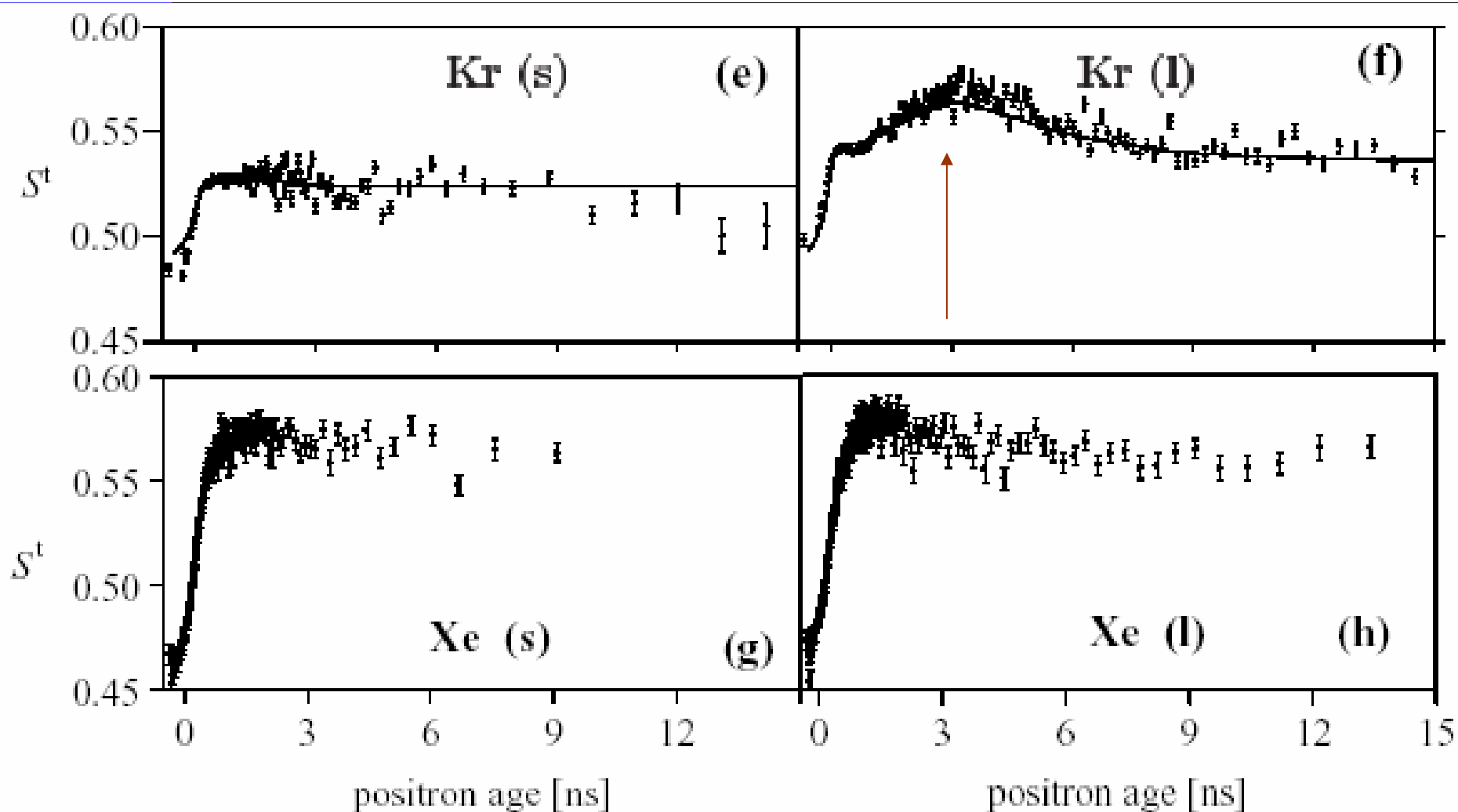


Fig. 8: Lineshape functions $S^t(t)$ calculated from AMOC data and model functions (solid lines) for condensed rare gases: Solid Ne at 15.2 K (a), liquid Ne at 26.0 K (b), solid Ar at 83.3 K (c), liquid Ar at 86.3 K (d), solid Kr at 50.0 K (e), liquid Kr at 120.0 K (f), solid Xe at 150 K (g), and liquid Xe at 163 K (h).

正电子的多普勒展宽 $S_t(t)$ 参数，在液态Ar和Kr中在3ns处有一极大值。分析表明，液态Ar和Kr中有Ps气泡从一个附加的delocalized亚稳o-Ps态中形成，结果还表明，液态亚稳o-Ps态寿命与固态在熔点附近的o-Ps寿命相同。在液态Ar和Kr中，跃迁到长寿命态或者到更稳的o-Ps气泡态的跃迁几率是 $3 \times 10^8/s$ 。在液体Ne中，线形参数在正电子寿命4ns-6ns区域有小峰表明可能有亚稳态Ps形成。实验同样表明，在Xe中没有发现有Ps气泡形成。

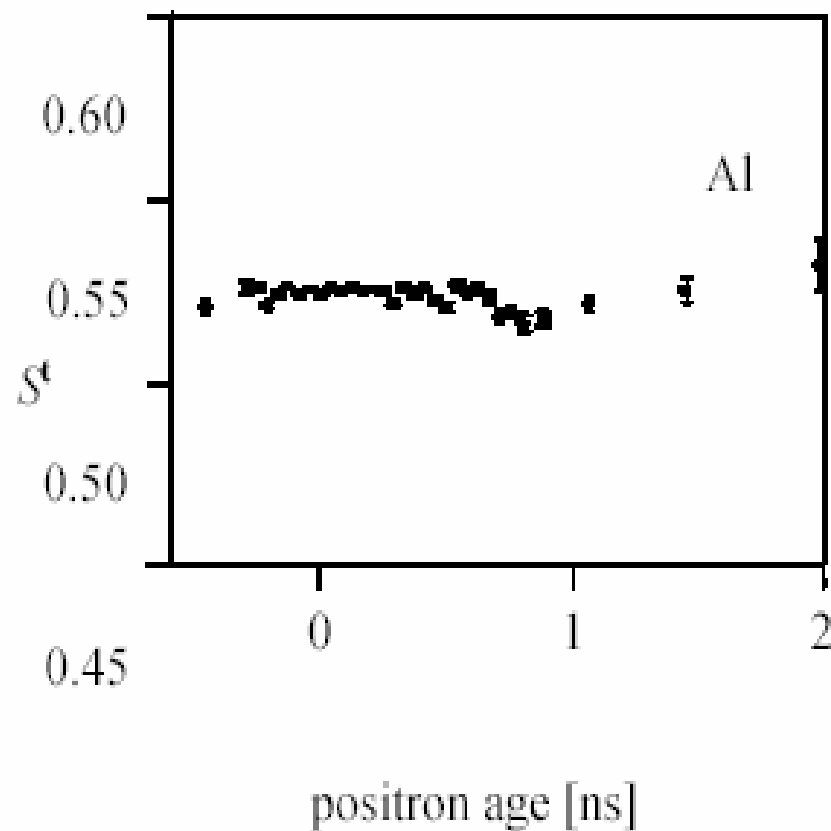
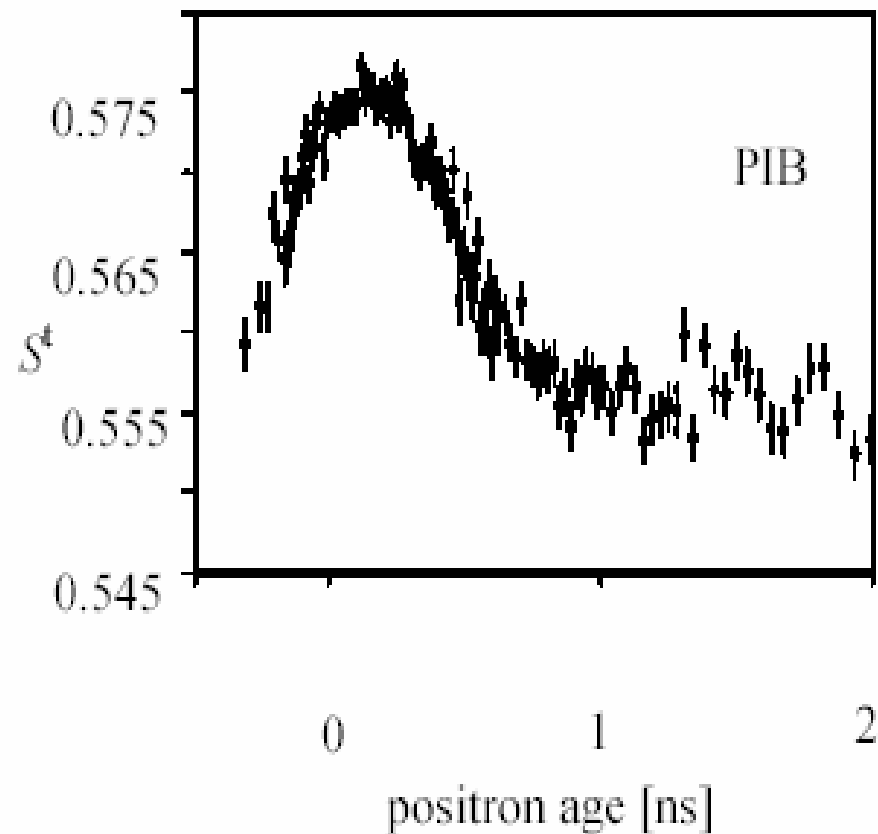




Ps热化

- Ps形成和热化过程是低能Ps物理和化学的基本课题，但在凝聚态中的Ps形成迄今还没有很好地了解。
- 例如，通过测量o-Ps的淹没可以了解多聚物的结构，这里就有一个关键问题：是否Ps形成是在预存在的位置（如，自由体积），或者Ps是否可以处处形成？当正电子能量较大时，通过碰撞将使气体分子或原子电离，这时Ps形成的几率就很小。仅当从气体分子中剥离一个电子的能量部分来自Ps的结合能 ΔE_{ps} 时，Ps形成在稀薄气体中才成为主要的去弹性碰撞道。
- 即对Ps形成，其正电子动能 E_{e^+} 必须落在Ore gap, 即： $\Delta E_{ps} > E_{e^+} > E_{e^+} - \Delta E_{ps}$ 。在凝聚态材料中，同样也存在Ore gap, 但Ps形成并不受该能隙的限制。

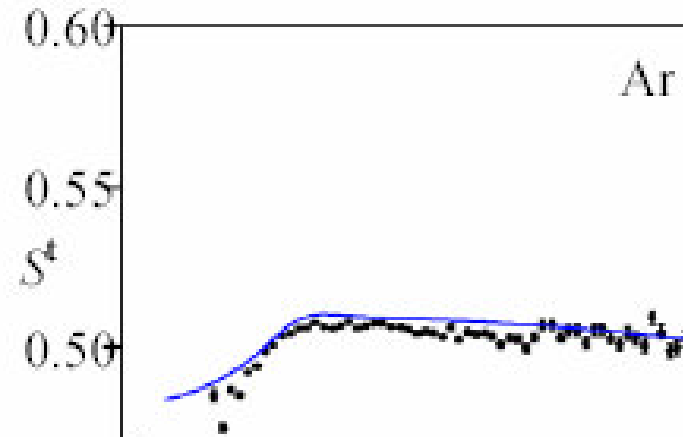
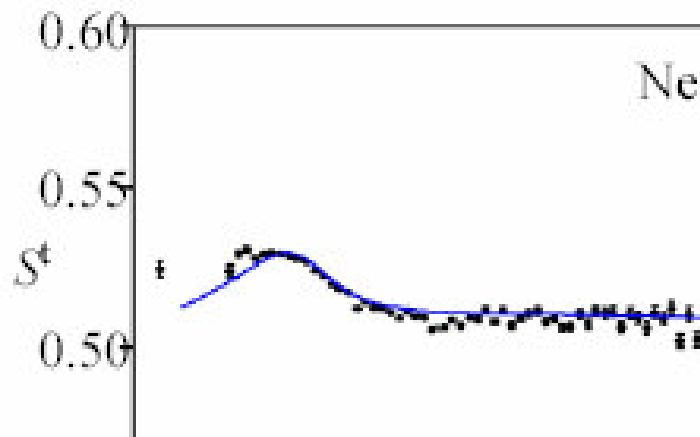




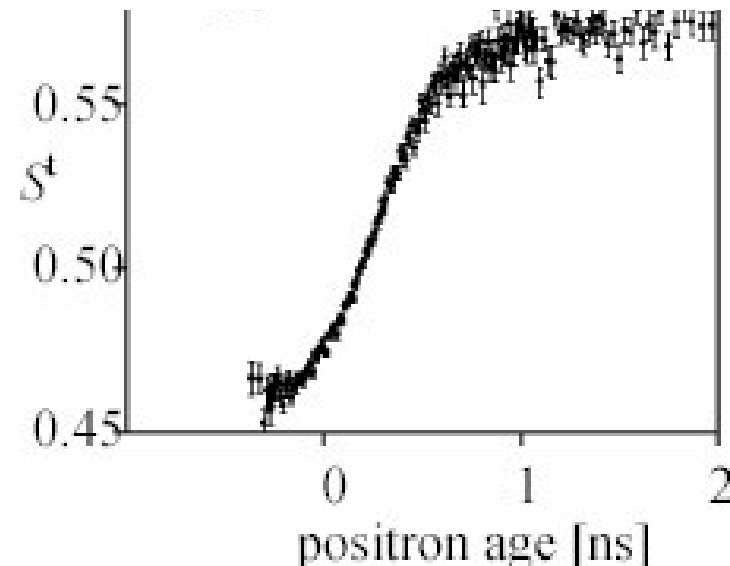
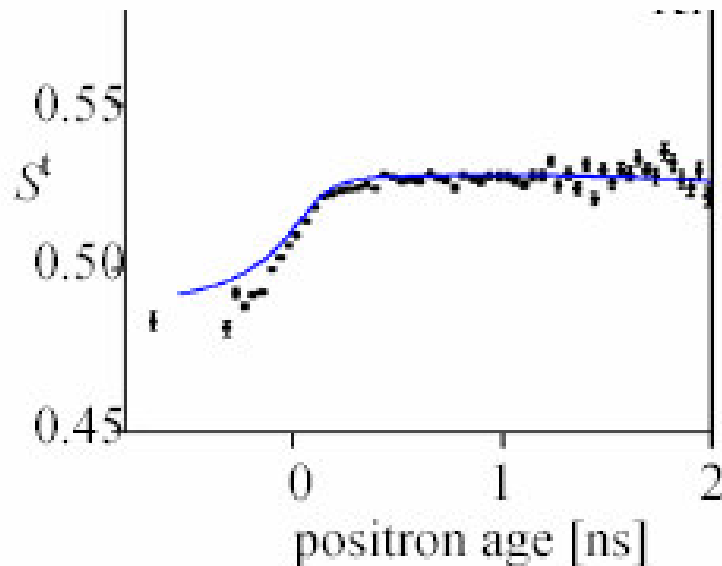
Polyisobutylene(PIB)

Al
表明金属中没有Ps形成





These materials crystallize in the face centered cubic (fcc) structure which, being a Bravais lattice, does not exhibit optical phonon branches. The lineshape functions $S^t(t)$ in Ar and, even more pronounced, in Kr and Xe show indeed a clear shift of the juvenile Doppler broadening to higher positron ages (Fig. 7).



- ② 迄今为止，所测量的在固体和液体中的Ps形成过程，都发现 S_t 在年轻时有一个峰值。如测量四甲基硅烷的 S_t 谱。而在其它无Ps形成的材料中，则就不能观测到这个峰值。如Al的 S_t 谱。AMOC数据的这种年轻展宽现象可以用二态模型来分析，在材料中，Ps的主要慢化过程是与光声子相互作用把能量传给晶格。Ps的能量损失过程允许超热Ps与热化Ps之间跃迁。基于束流的AMOC可以用研究Ps在凝聚态材料中的热化过程。
- ② 表I表明了p-Ps和o-Ps热化湮灭的各种特性。



表I AMOC实验中不同正电子态的湮灭特性

	热化p-Ps	非热化p-Ps	o-Ps pick-off湮灭	自由e ⁺
正电子寿命	年轻	年轻	老	中间
多普勒展宽 $\Delta E\gamma$	小	大	大	大
S-参数	大	小	小	小

Ps和正电子化学

- Ps态由于氧化、复合和自旋转换等过程将产生不同Ps态之间的跃迁，即所谓的Ps反应。这种过程导致一个更短的o-Ps寿命并改变正电子-电子对的湮没动量。AMOC技术就可以观察这种不同Ps态之间的跃迁，例如，在HTMPO材料中o-Ps转化为p-Ps引起在年长区（old positron age） $S_t(t)$ 的增加。
- 用AMOC技术，人们还发现，当自由正电子与水溶液中卤化物离子反应时，在一定寿命区域观察到比纯溶液更窄的多普勒展宽现象。这种过程表明AMOC技术可以把正电子与卤化物离子反应和Ps反应区别开来。



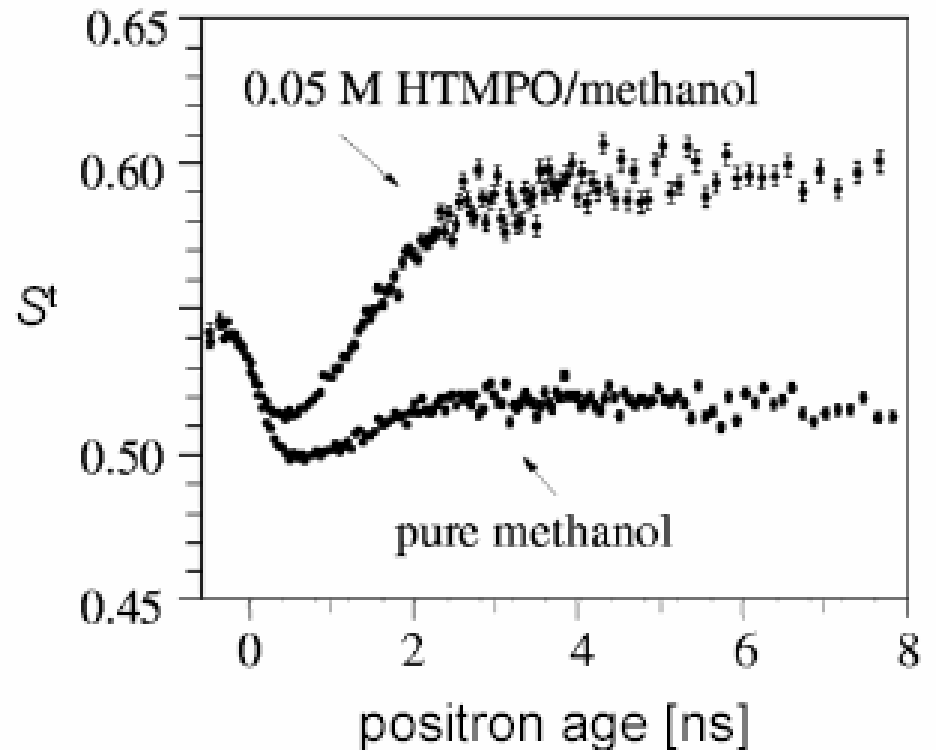
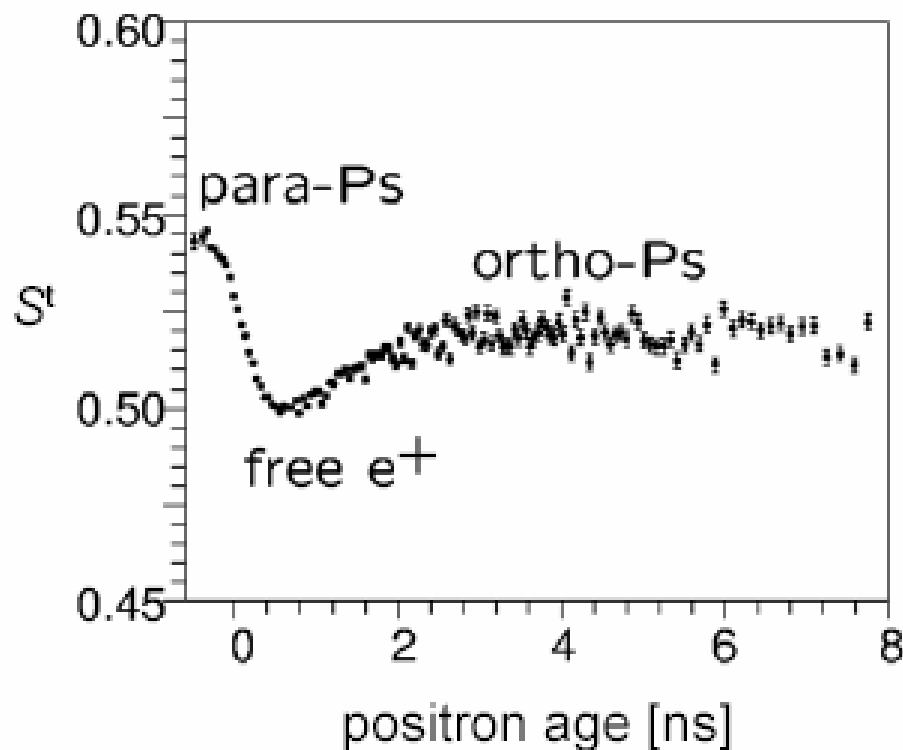


Fig. 3: Left side: Lineshape function of methanol. The time-dependent S -parameter is determined by the narrow momentum distribution of short-lived para-positronium, the momenta of the electrons annihilating with positrons not forming Ps (free e^+), and the “pick-off” annihilation of long-lived ortho-positronium (annihilation of the positron of o -Ps with a “foreign” electron). Right side: The free radical HTMPO dissolved in methanol causes a significant increase of S^t at old positron ages since long-lived o -Ps is converted to p -Ps showing its characteristic small Doppler broadening (corresponding to a high S -parameter) of the annihilation radiation.

正电子捕获率

Lauff and Nilen 研究了 **diamond** 在光照射下的正电子捕获率，他们测量了 **diamond** 的 **AMOC** 谱，用两寿命分量拟合 **AMOC** 数据，得到了正电子捕获率在白光照射下几乎大一倍的结论。

	$K [10^9 / \text{s}]$	$\tau_f [\text{ps}]$	$\tau_t [\text{ps}]$
light on	1.4	115	386
light off	0.7	115	358



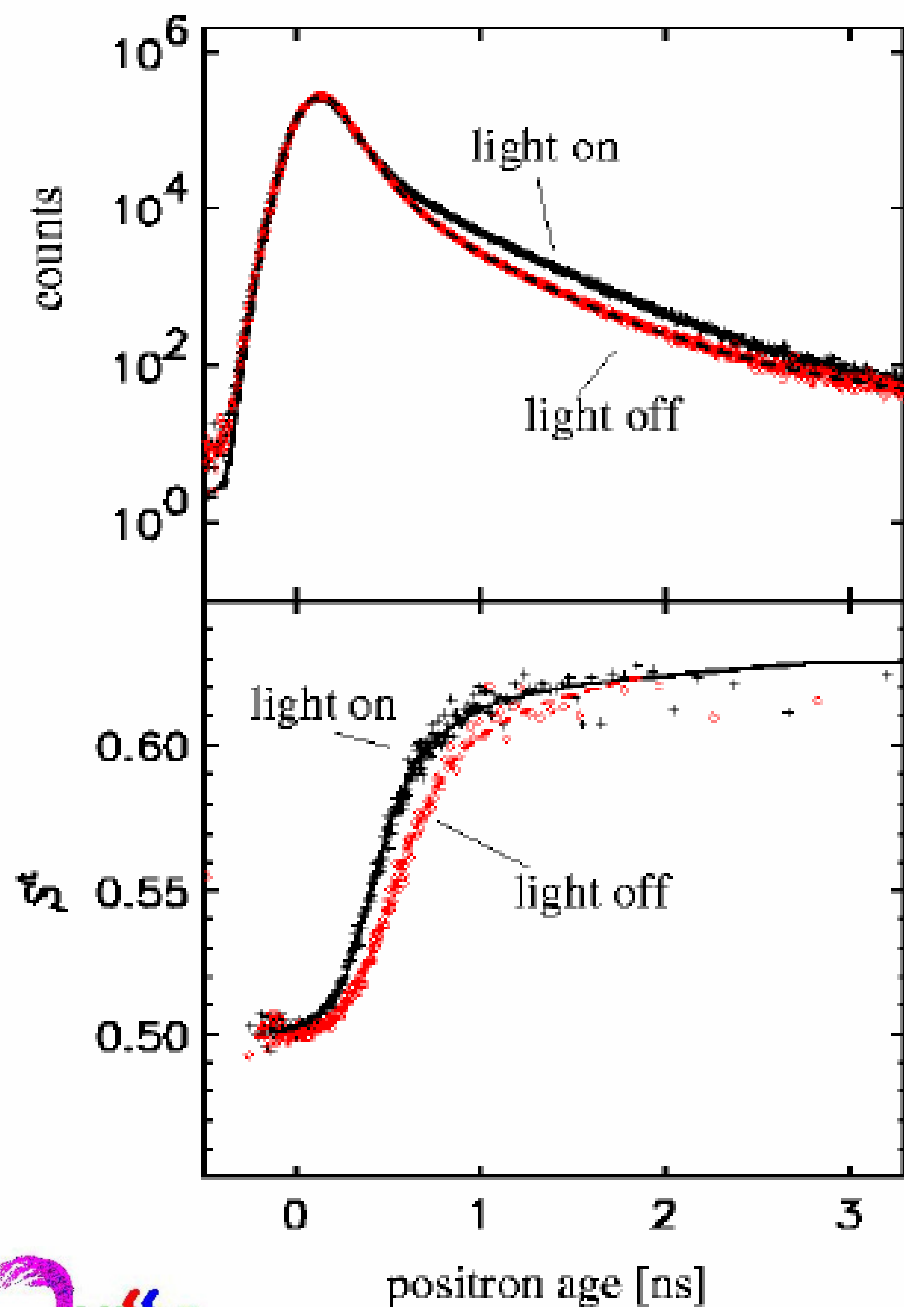


Fig. 4: Positron-lifetime spectrum (upper diagram) and lineshape function $S'(t)$ (lower diagram) of a natural type IIa diamond. Influence of white light. The solid and dashed lines represent fits of a two state trapping model. Parameters are given in Table 1.

用AMOC测量p-Ps寿命

- 2000年日本 N.Suzuki用AMOC技术测量了p-Ps寿命。
- 测量原理：

$$S(t) = \frac{\int_{\pm \Delta p} N(p, t) dp}{\int N(p, t) dp} = \frac{\int_{\pm \Delta p} N(p, t) dp}{L(t)},$$

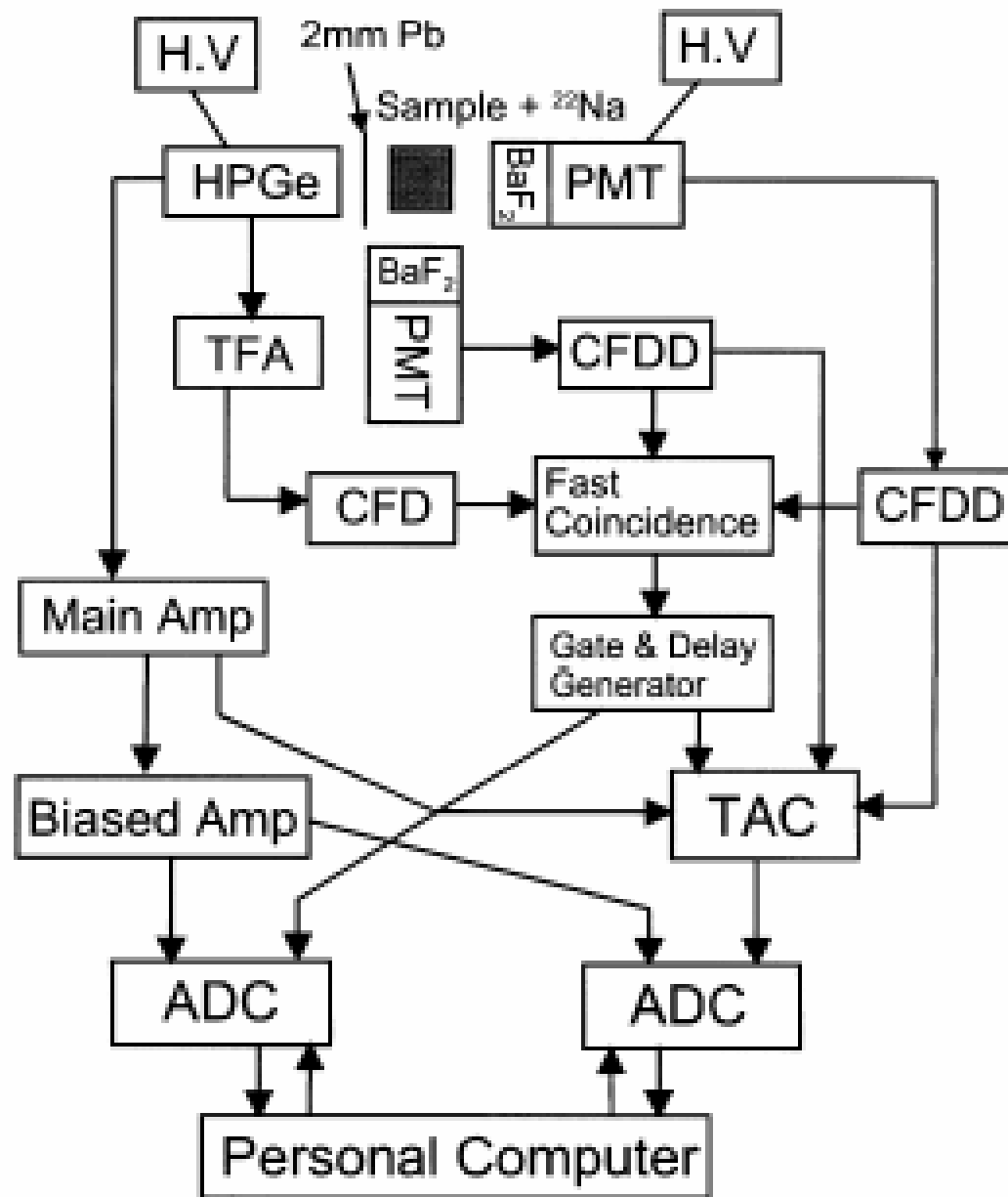
$$S(t) = \frac{\sum_{i=1}^n S_i \cdot l_i(t)}{L(t)}, \quad L(t) = \sum_{i=1}^n l_i(t) = \int N(p, t) dp,$$



让**n=2**, 且第**2**寿命大于第**1**寿命, **S**
(**t**) 的时间平均主要是**S₂**贡献。

$$l_1(t) = \frac{S(t) - S_2}{S_1 - S_2} \cdot L(t) \propto (S(t) - S_2) \cdot L(t).$$





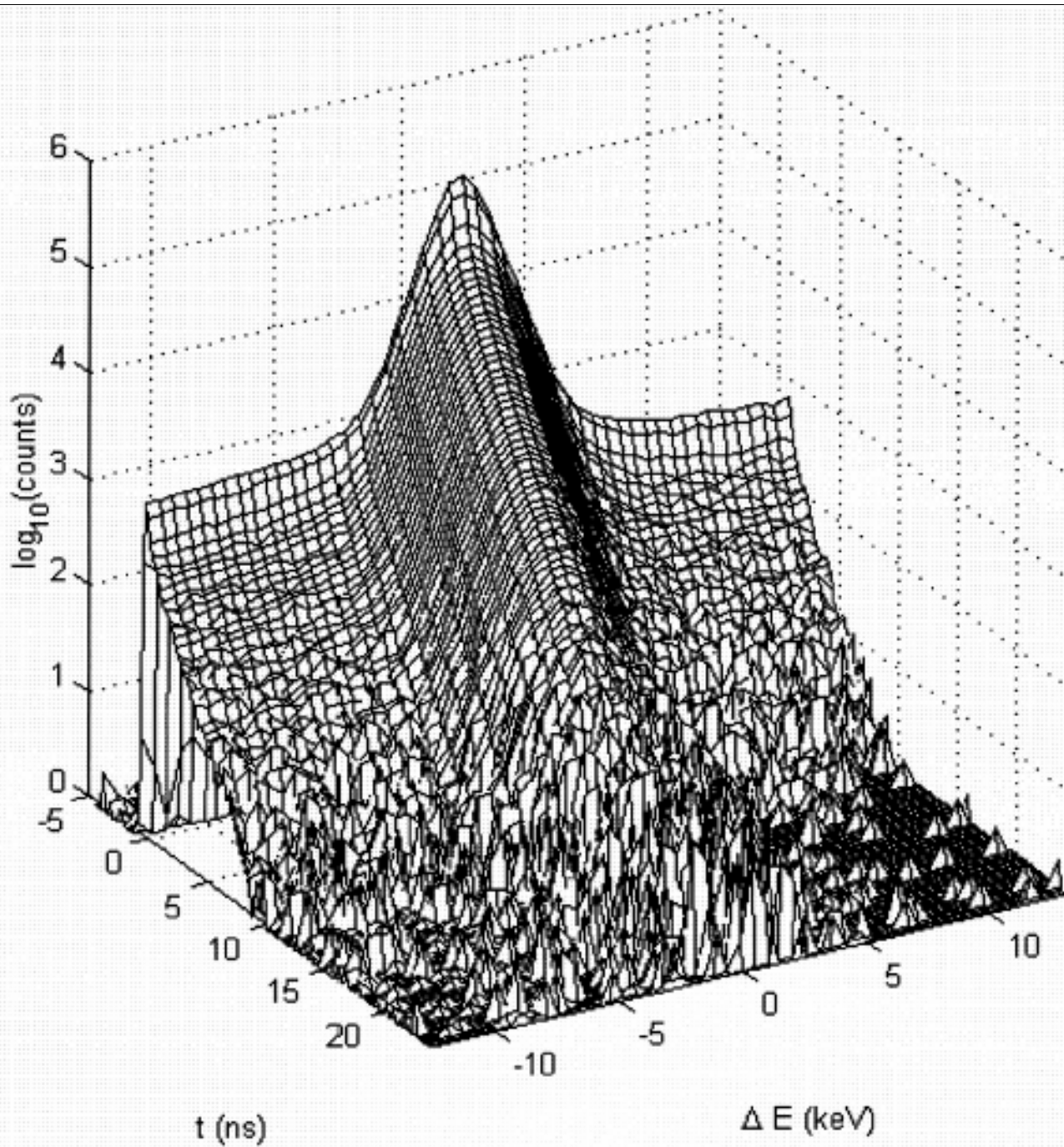
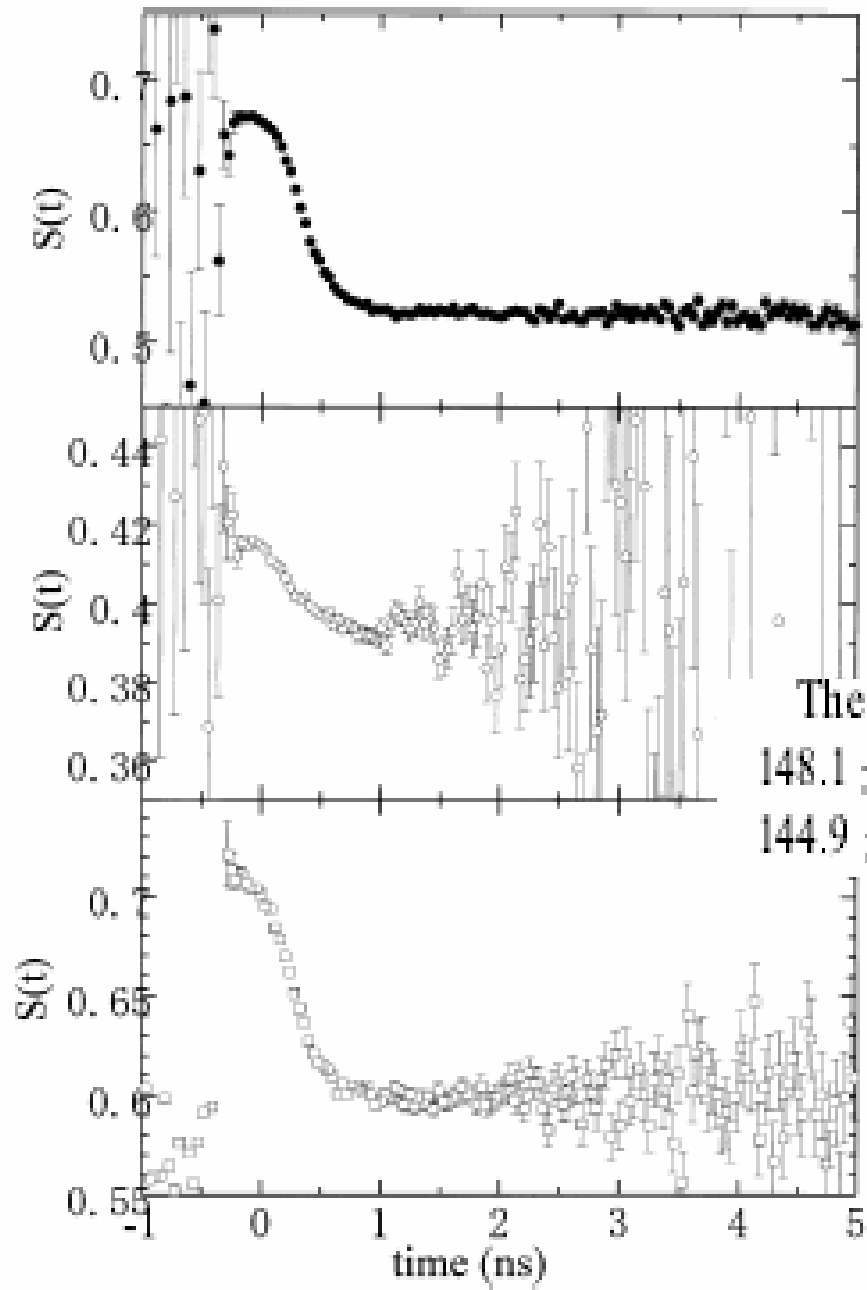


Fig. 2. AMOC spectrum for a-SiO₂.





The shortest lifetimes obtained from the fitting are 148.1 ± 1.0 ps for a-SiO₂, 111 ± 6 ps for α -quartz and 144.9 ± 2.4 ps for SiO₂ powder. The errors include

Fig. 3. Time evolution of $S(t)$ for a-SiO₂, α -quartz, SiO₂ powder.



- ☯ 1999年他们已经作了类似的工作，测量了Zn的在不同温度下的AMOC谱，分析和重构数据，得到了短寿命分量随温度的变化。

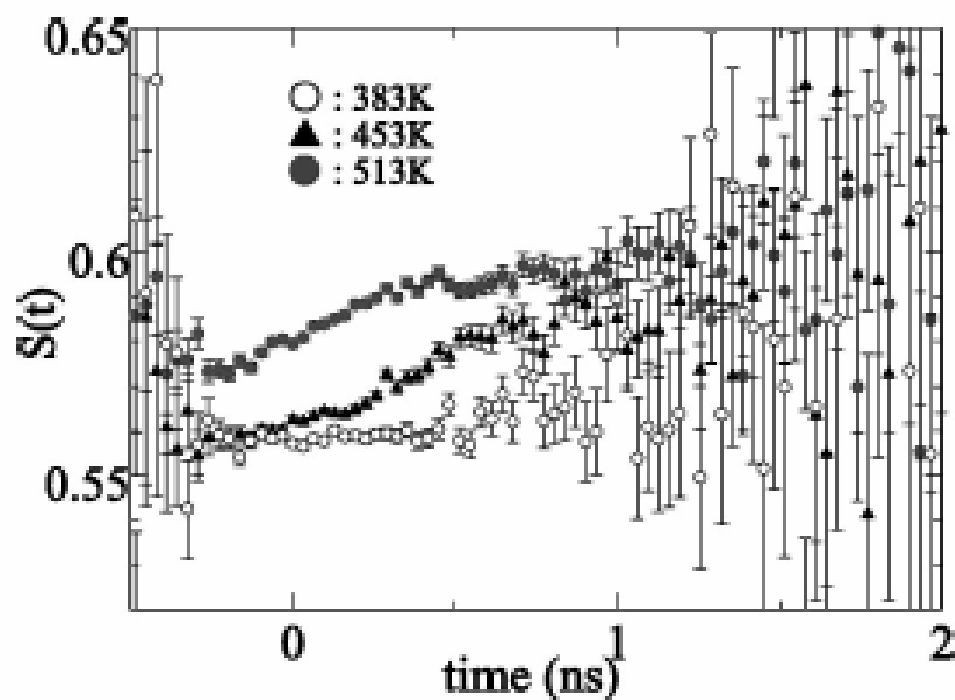


FIG. 2. Time evolution of $S(t)$ for Zn at 383, 453, and 513 K.



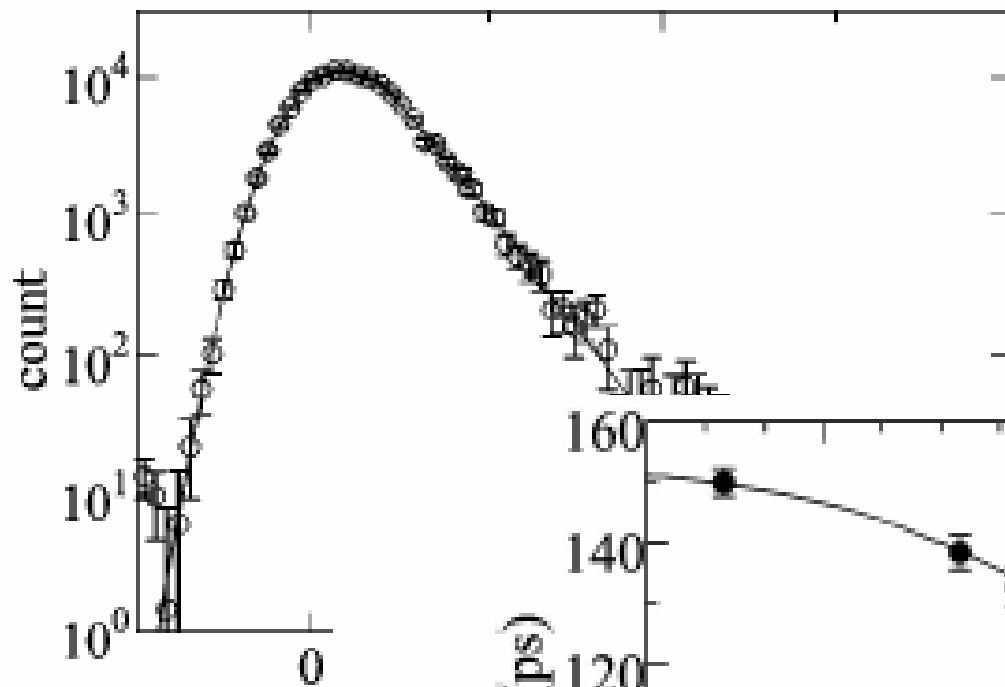


FIG. 3. Reconstructed lifetime component for [unclear]

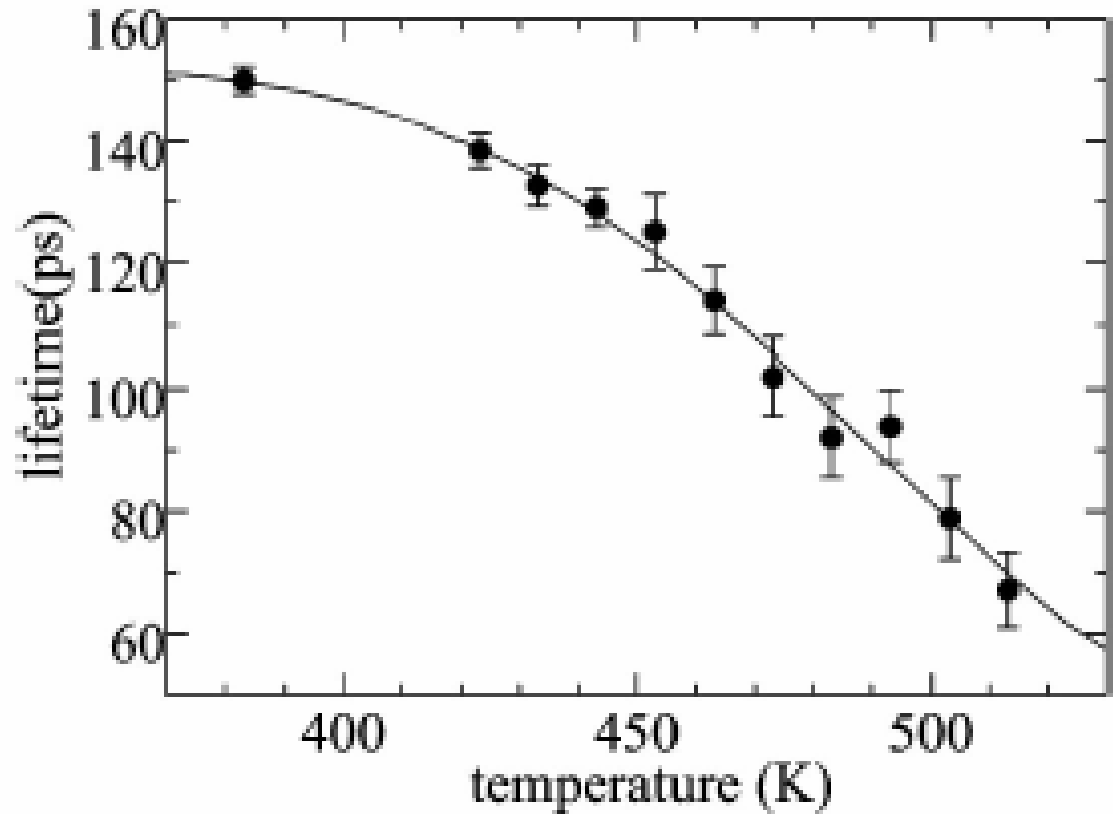


FIG. 4. The short lifetime τ_1 plotted against the temperature.



固体空位形成能

- 基于正电子AMOC技术还有许多其他应用，如最近日本东京大学的N.Suzuki等人采用了AMOC技术，测量了固体In, Zn的空位形成能 E 。他们所采用的方法与以前人们所使用的方法具有较大的不同，他们测量了不同温度下的 S_t ，采用了二分量最小二乘法分析和外推，得到了空位形成能 E_D 。



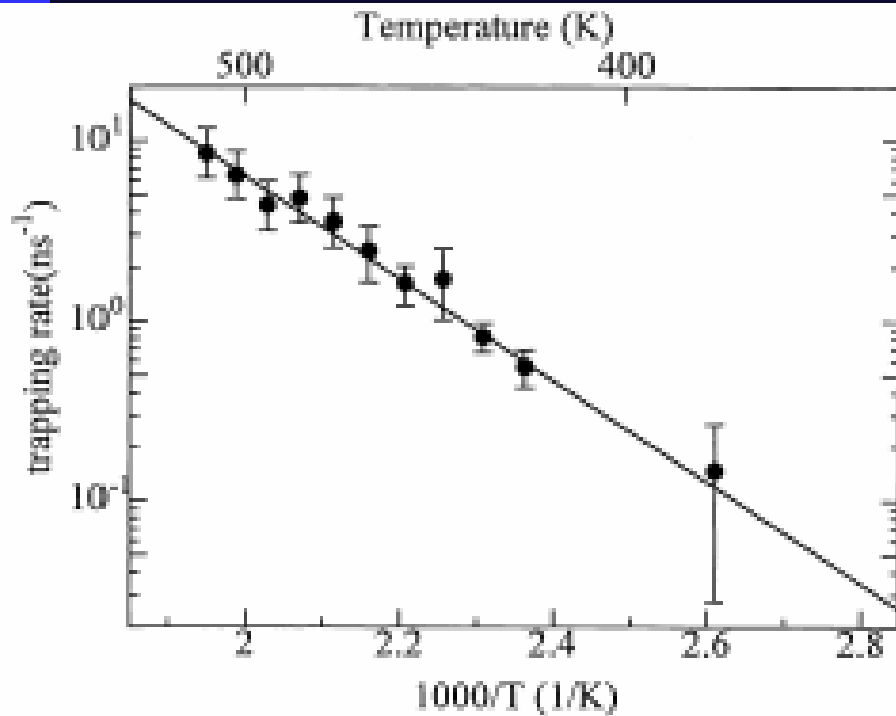


Fig. 4. Temperature dependence of the positron trapping κ in Zn vs temperature.

2000年Hyodo测量了单空位形成能，起方法同上，得到了正电子捕获率随温度的变化，由捕获率与温度与空位形成能的关系拟合得到了空位形成能。

$$\kappa \propto e^{-E_D/k_B T}$$

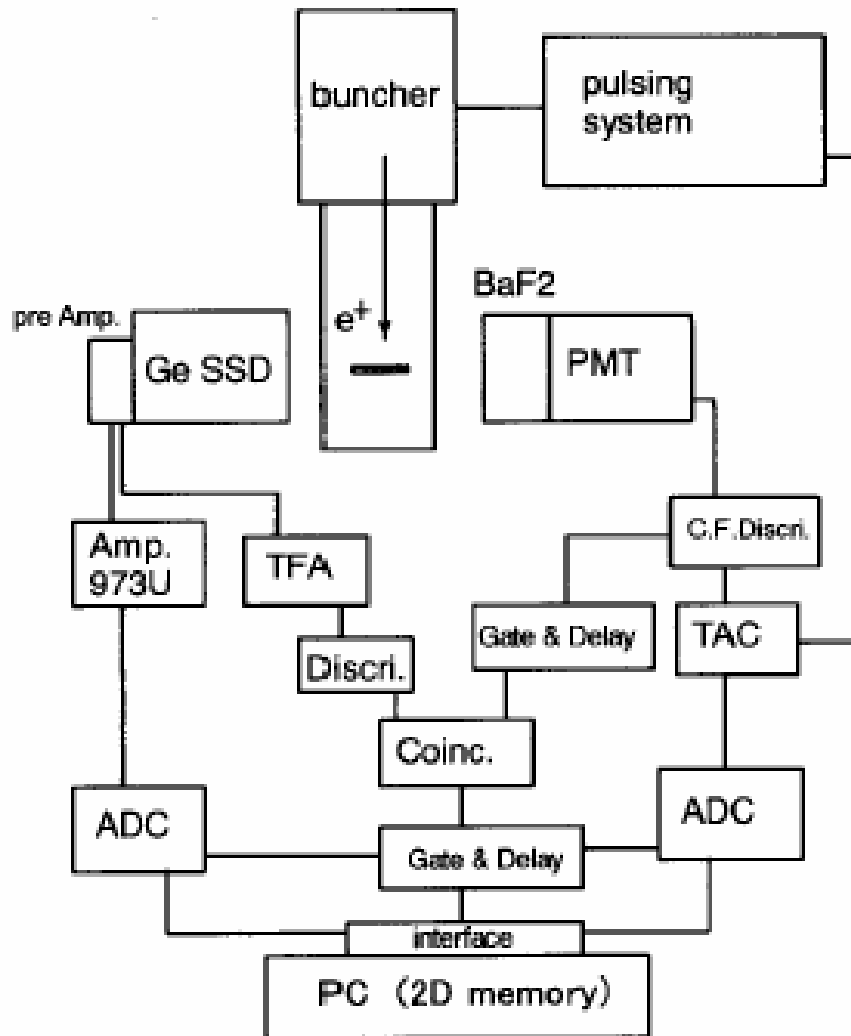


AMOC发展

- ❖ 与慢束结合
- ❖ 探测技术改进
- ❖ 分析手段完善
- ❖ 拓宽研究领域



与慢束结合



2001年R.Suzuki发展了一台基于脉冲化的慢束系统的AMOC，慢束强度为 $10^8 e^+/s$ ，能量从0.3-25keV，最大符合计数率达到2000cps.

The pulse-stretched beam is then short-pulsed to ~ 150 ps by a pulsing system developed for positron lifetime measurements [5]. The positron energy is variable from 0.3 keV to 25 keV, and the pulse interval is variable from 26 ns to infinity with 26 ns step.

探测技术改进

- 多探测器
- 数字化



分析手段完善

- ☯ 二维含时分析
- ☯ 动量与时间的关联



Thank you!